Application and Development of 2D IR Spectroscopy for the Study of Complex Biological Systems

Mark Cheng

A dissertation
submitted in partial fulfillment of the
requirements for the degree of

Doctor of Philosophy

University of Washington
2013

Reading Committee:
Munira Khalil, Chair
Dennis M. Heinekey
Philip J. Reid

Program Authorized to Offer Degree:
Chemistry

University of Washington

Abstract

Application and Development of 2D IR Spectroscopy for the Study of Complex Biological Systems

Mark Cheng

Chair of the Supervisory Committee:
Assistant Professor Munira Khalil
Chemistry Department

One of the many applications of 2D IR spectroscopy is in the study of structure/function relationships in proteins. While this technique can be used for structural characterization, the power of this tool is with its ability to provide timescales for the structural dynamics of a system in solution with picosecond time resolution. It is in this manner that 2D IR was used to understand the pH-dependent release mechanism of nitric oxide in the heme protein Nitrophorin-4. By probing the vibrational stretch of the nitrosyl ligand as a function of time, shifts of the vibrational stretch report time-dependent changes of the local electric field around the ligand and its interaction with the ferric heme center. The timescales extracted indicate that the ligand is sensitive to pH-dependent changes to the local distal pocket environment and to two distinct conformations of the protein.

While this protein has numerous vibrational modes, the limited bandwidth (~250 cm^{-1}) of the mid-IR source confined the spectral window to the nitrosyl stretch. To overcome this limit for future studies, a tunable and spectrally broad mid-IR pulse source was developed. This new source generates sub-20 fs, octave-spanning ($> 2000\ \mathrm{cm}^{-1}$) broadband mid-IR pulses and is tunable from 2–8 μm. These mid-IR pulses are generated by four-wave mixing during the filamentation of intense 800 nm and 400 nm pulses in various gas media. Spectral tunability is

achieved by the choice of gas, pressure and input 800 nm pulse energy. Pulses from this source would allow one to coherently probe numerous vibrations, potentially revealing correlations between local and global structural fluctuations.

TABLE OF CONTENTS

Chapter 1: Introduction

Chapter 2: 2D IR Spectroscopy of Nitrophorin 4

Introduction

Methods

Results

Discussion and Conclusion

Future

Chapter 3: Development of a Tunable Ultra-Broadband Mid-IR Pulsed Source

Introduction

Setup

Results

Discussion and Conclusion

Appendix

Chapter 4: Integration of Broadband IR Source in a Multidimensional Spectroscopy Setup

Introduction

Implementation of BBIR Probe in the Experimental Setup

Preliminary IR Pump-BBIR Probe Spectroscopy of the Benzoic Acid Dimer System

2D IR Spectroscopy with the BBIR Source

Appendix

List of Figures

List of Tables

Table Number Page

Glossary

χ^{3}_{jjjj}	Third-Order Nonlinear Susceptibility
$\delta\omega$	Time-Dependent Frequency Fluctuation
π/T_2^*	Homogenous Linewidth
$T_{vib,lif}$	Vibrational Lifetime
ν	Vibrational Stretch
1D	One Dimensional
2D	Two Dimensional
4WM	Four-Wave Mixing generation
BA-d$_5$	Deuterated Benzoic Acid Dimer
BBIR	Broadband mid-IR
CLS	Center Line Slope analysis
DFG	Difference Frequency Generation
FFCF	Frequency-Frequency Correlation Function
FT	Fourier Transform
FTIR	Fourier Transform Infrared Spectroscopy
FWHM	Full-Width at Half Maximum
g(t)	Lineshape Function
HeNe	Helium-Neon
IR	Infrared Spectroscopy
LO	Local Oscillator
MCT	Mercury Cadmium Telluride
ND	Neutral Density filter
NO	Nitric Oxide
NP4	Nitrophorin-4
NP4-NO	Nitric Oxide bound Nitrophorin 4
OPA	Optical Parametric Amplifier
P_j^3	Third-Order Nonlinear Polarization
$R^1(t)$	Linear Response Function

SNP	Sodium Nitroprusside
TTL	Transistor–Transistor Logic
UV-Vis	UV-Visible Spectroscopy
VI	Virtual Instrument
XFROG	Cross-Correlation Frequency Resolved Optical Gating

Acknowledgments

The first step into the Bagley Hall, room 95 in the summer of 2008 was a very scary and intimidating moment. However, all the anxiety that was felt in that instant never matched the excitement of being part of something new. Being down in the labs for most of my graduate career (if not, my life for the past 5 years), I was glad to have shared some of the ups and downs with those whom I worked with to make these labs grow. Mike and Stephanie, thank you for being the “marines” of the lab by getting things started. They were followed by the calvary that I was grateful to be a part of: Anthony, Karla, Jason and Heather. Last but not least, thank you Munira, for your endless and contagious enthusiasm and for being an exemplary scientist for all of us to follow.

Graduate school was not easy, but I never imagine it do be as difficult as it was. Strangely, the unconventional path that I took in the years leading up to graduate school had prepared me well. It provided me many reminders of who I am and what I am capable of. If not for this, I would have been completely crushed. Thus, I am eternally grateful to numerous individuals for all they have taught and given me. To Cathy, Hemant, Patty, Marilyn, Helena, the Alex-es, Susan and everybody else at RSM, thank you for teaching me the meaning of hard work, team work and how to lighten up! To Clifford, Dan, Esther and Janaki, thank you for instilling a deep appreciation for the wonders of biology. To Giselle, Illeana, Stephanie and all the educators and staff at ESCHS, thank you for teaching me the true meaning of “dedication.”

To Leanne and David, thank you for taking a chance with me and all the wonderful memories that I have from being part of MGI/Gear UP and UWMSUB. To Dr. P. Johnson, Dr. F Raineri and Dr. S. S. Wong, thank you for your endless support and belief. To Roberto and Danielle, thank you for your infinite wisdom about the mind, body and spirit. Last but not least, to all the students that I had the good fortune of working with over the last several years, thank you for sharing your stories and your struggles with me. You were all truly inspirational and I was glad that we were able to learn much from one another.

Finally, to mom, dad and my brother, as well as all my friends and family here, back east (in New York) and in the Far East (in Hong Kong), I hope you are proud.

Dedication

To the East Side High School class of 2012,
thank you for reminding me how to be a good student.

To the students of the 2013 UWMSUB program
from Chief Sealth, Cleveland and Franklin class of 2014 and 2015
thank you for reminding me the joys of science.

To Augustine and Sumiko Patrone,
thank you for your mentorship, unlimited patience and
for teaching me the meaning of being
one of Earth's children.

Chapter 1

Introduction

1.1.1 Overview

The work done with ultrafast 2D IR spectroscopy in the past decade has demonstrated that the use of femtosecond mid-IR pulses can provide much insight into the solution phase structural dynamics on the picosecond time scale for a variety of systems, ranging from molecules of water to macromolecules of proteins [1-5]. Although the questions that are addressed with regards to energy transfer and structural dynamics are fundamental to chemistry, the answers are often pertinent to many other fields. For instance, understanding electron or proton transfer process of an inorganic molecule would enable a material scientist to design more efficient solar material and inquiry into the structural dynamics of a protein is crucial for a biochemist to determine the origin of its function [6, 7].

1.2.1 Infrared (IR) Spectroscopy of Proteins

Linear Fourier transform infrared (FTIR) spectroscopy has been (and still is) extensively used to study biological systems [8-12]. Analysis of spectra of polypetides and proteins can yield information such as bond lengths and bond strengths, the protonation state of side chains, the strength of the hydrogen bonds and the structural heterogeneity of the sample in the given solvent [13-18]. This information is often buried under broad and featureless lineshapes and analysis methods such as band-fitting techniques or second derivative methods are used to resolve the individual components. However, these methods are ineffective as the complexity and size of the system increases [19].

The technique of 2D IR spectroscopy yields spectra that permit the extraction of such information more readily. Overlapping bands hidden under broad 1D lineshapes in a linear FTIR spectra are decongested by spreading spectral features across two frequency axes and features additional details (such as anharmonicities) that can be read off directly from the 2D spectra [9, 20-23]. Moreover, the ability of this method to coherently probe the coupling between the different vibrational modes of a protein reveals cross-peak features that are absent with linear FTIR spectroscopy.

1.3.1 Two Dimensional Infrared (2D IR) Spectroscopy of Proteins

2D IR spectroscopy is a third order nonlinear spectroscopy technique that employs a sequence of three mid-IR pulses (as illustrated in figure 1.1(a). The interaction of these three pulses (separated by three time periods: τ_1, τ_2 and τ_3) with a sample generate a vibrational echo signal. The first pulse establishes a vibrational coherence and is allowed to evolve during τ_1. A second pulse is then introduced and changes the vibrational coherence into a vibrational population. After some time τ_2 has elapsed, a third pulses is introduced. This pulse reestablishes a vibrational coherence and a resultant vibrational echo is emitted. The emitted vibrational echo is heterodyne detected to preserve the time and phase information.

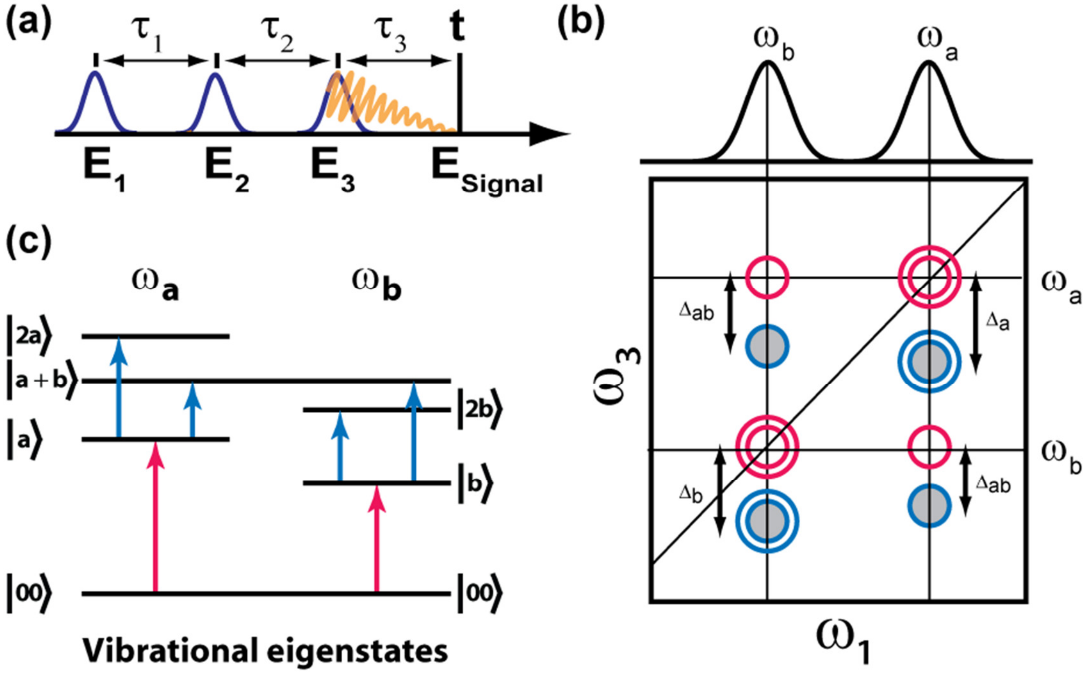

Figure 1.1. (a) An illustration of a 2D IR pulse sequence and the time delays that separate the pulses. (b) A cartoon of a 1D and 2D spectrum of two-coupled vibrations. The unshaded and shaded areas represent positive and negative peaks respectively. The splitting between these features is a direct measure of the vibrational anharmonicities ($\Delta_{a,b}$ and Δ_{ab}). (c) An illustration of the vibrational eigenstates that are represented in the cartoon 2D spectrum.

A 2D IR spectrum maps the correlation of frequencies detected during the first time periods τ_1 and τ_3. In order to produce spectra in the frequency domain, the collected data is Fourier transformed along the time period τ_1 to yield the ω_1 axis, while the ω_3 axis is obtained by spectrally dispersing the signal with a monochrometer and detecting the dispersed frequencies at the focal plane of a liquid N_2 cooled HgCdTe array detector. Figure 1.1(b) is a cartoon illustration of a 2D IR spectrum for a coupled multilevel vibrational system.

The different vibrational modes (ω_a and ω_b) of a molecule are mapped out along the diagonal axis while cross-peaks (along the off-diagonal axis) are indicative of coupling among the different vibrational modes (ω_{a+b}). The positive and negative features are representative of the $0 \rightarrow 1$ and $1 \rightarrow 2$ transitions and the separation between these two peaks is a direct measurement of the vibrational anharmonicity.

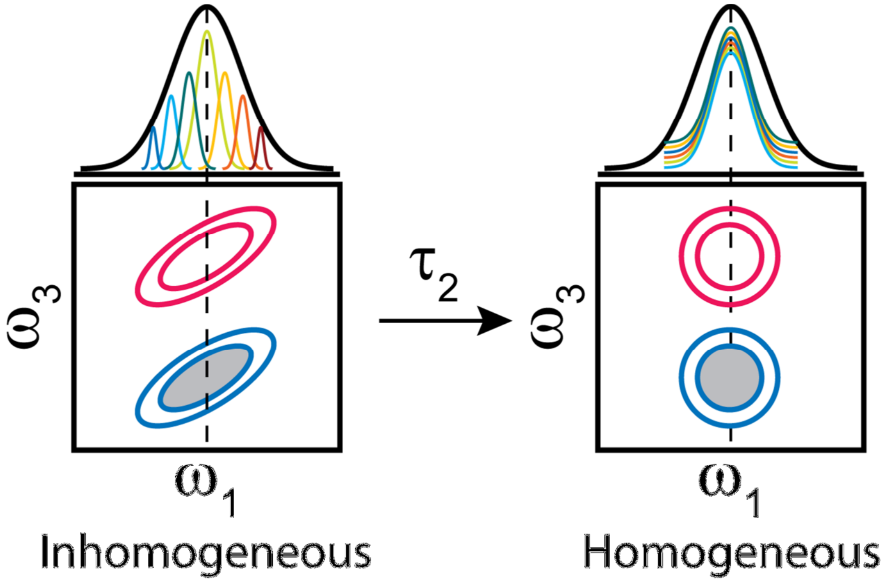

Figure 1.2. An illustration of how 2D IR lineshapes can disseminate the degree of inhomogeneous broadening. While there are there are no discernible differences in the 1D lineshapes between completely inhomogeneous and homogeneous dynamics, 2D lineshapes are completely elongated or symmetric (respectively) at these two limits.

Furthermore, the 2D lineshape of each spectral feature can be analyzed for information regarding the dynamic nature of the vibrational mode with its surrounding environment. Figure 1.2 illustrates how the ellipticity of the 2D lineshapes reflects the degree of inhomogeneous broadening. Monitoring the change of the 2D lineshape as a function of τ_2 yields timescales for dynamic process such as vibrational relaxation and spectral diffusion.

It is in this manner the timescales of the pH-dependent structural dynamics of the nitrosyl (NO) ligand in the hemeprotein Nitrophorin-4 (NP4) were measured. NP4 functions as a container and transporter of nitric oxide and has been extensively characterized and studied due to its importance in numerous biological processes [24-26]. While past studies on NP4 focused on the pH-dependent secondary structural changes and the polarity of the distal pocket differences among its two conformations, the release mechanism has never been studied from the point of view of the ligand. Analysis of evolving 2D lineshape of the nitrosyl stretching vibration (ν_{NO}) report changes of the local electric field and Fe-NO bonding interactions in the open and closed conformers. These conformers are present at low (pD 5.1) and high (pD 7.9) conditions and are represented by two distinct NO stretching vibrations.

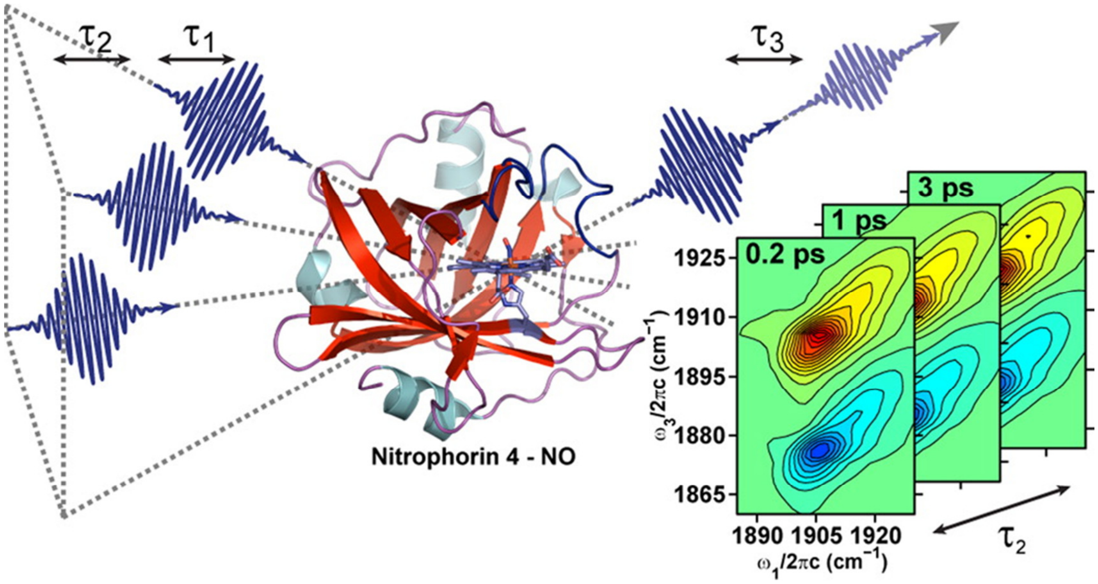

Figure 1.3. A cartoon illustration of the 2D IR NP4-NO experiment. A selection of the 2D IR spectra (shown on the right) highlight the evolution of the spectral features as a function of τ_2. Changes to the spectral features report the structural fluctuations experienced by the NO ligand.

Analysis of the evolving 2D lineshapes revealed two timescales for the NO structural fluctuation in each conformation regardless of the pD environment: a fast ($\tau_{c1} \leq \sim 3$ ps) and a slow ($\tau_{c2} \geq \sim 70$ ps) component. The fast (τ_{c1}) timescales were attributed to fluctuations of the local electric field around the nitrosyl ligand in NP4-NO. The difference of this τ_{c1} timescale reflects the hydrophobic and hydrophilic character of the distal pocket, which has implication in the dissociation/rebinding of NO from the heme [27, 28]. The slow (t_{c2}) frequency fluctuations were attributed to the structural dynamics of pH-sensitive secondary structural elements. At both pD, the closed conformers maintain a static distribution of vibrational substates (for ν_{NO}) within the experimental time window. In contrast, the vibrational substates were able to interconvert in the open conformer on a ~ 100 ps time scale. Differences in the τ_{c2} timescales reflect the "flexibility" of these structural elements that govern ligand escape to the solvent from the distal pocket.

Although the 2D IR nitrophorin study was focused mainly on the nitrosyl stretching vibration, there are many other vibrational modes that can be probed as well. Among them are the Amide I and Amide II normal modes that are sensitive to secondary structure elements. Given that these elements may have "inherent dynamic properties," the study of secondary structure may explain why nitrophorin (comprised of β-sheets) has a different release mechanism from myoglobin (comprised of α-helices) [29]. 2D IR has been demonstrated to be a useful tool in study of secondary structure since coupling between the Amide I and Amide II modes result in cross-peaks spectral features that are more sensitive to secondary structure elements than probing either region alone [30-32]. Thus, there is a wealth of information that 2D IR studies can provide by simultaneously monitoring the local structural fluctuations around ν_{NO} and the global structural fluctuations of two ν_{amide} [30, 32, 33].

The use of a tunable and spectrally broad mid-IR probe would permit such study and may reveal correlations between the local and global secondary structural fluctuations [34-36]. Broadband mid-IR (BBIR) pulses are typically generated by the filamentation of intense femtosecond 800 nm pulses and its harmonics in gases at ambient pressure [34, 35, 37-41]. Pulses generated in this manner have spectral bandwidth $\Delta_{\omega_{\mathrm{FWHM}}} > 2000\ \mathrm{cm}^{-1}$, whereas the established method of generation with an optical parametric amplifier (OPA) and difference frequency mixing (DFG) in various nonlinear IR crystals result in pulses with spectral bandwidths ($\Delta_{\omega_{\mathrm{FWHM}}}$) of $\sim 250\ \mathrm{cm}^{-1}$ [42]. The aspect of tunability comes from containing the filamentation of 800 nm/400 nm (ω/2ω) light fields within a gas cell. By controlling the gas medium (air, Ar, Ne, and N_2) and its pressure, the source can generate sub-20 fs, octave-spanning BBIR pulses tunable from 2–8 μm with spectral width greater than 2000 cm^{-1} [36].

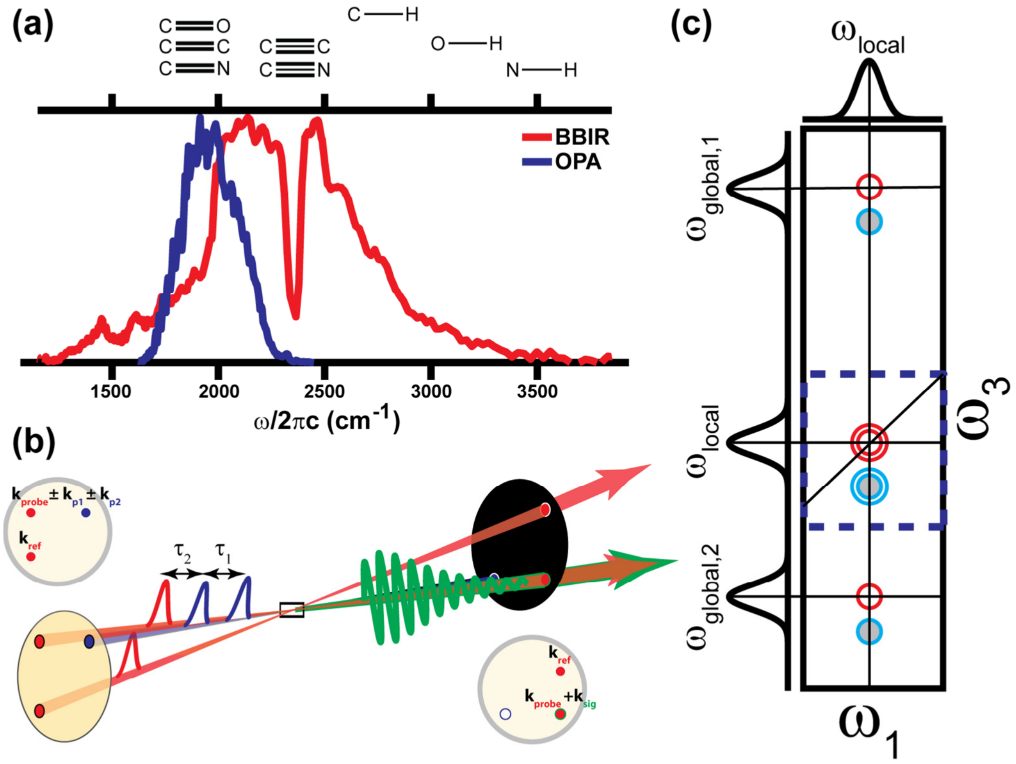

Figure 1.4. (a) Comparison of the spectral bandwidth of a mid-IR pulse from an OPA/DFG setup and BBIR generation in 406 Torr of air. (b) The pulse sequence the employs narrowband pulses from an OPA/DFG (blue) and BBIR (red). (c) Cartoon illustration of the resultant 2D IR spectrum. The dotted box highlights the limited vibrational coherences that can be probed with a narrowband pulse.

1.4.1 Thesis Outline

This thesis chronicles the work that has been done over the years and begins with an example application of 2D IR spectroscopy for the study of biological systems. This technique was used to study the pH-dependence of nitric oxide storage and transport in the hemeprotein Nitrophorin-4. It will then move onto the development and characterization of spectrally broad and tunable mid-IR source. By containing the filamentation of the fundamental and its harmonic within a gas cell, spectrally broad pulses (> 2000 cm^{-1}) can be generated and tuned to a particular spectral region by controlling the content and pressure of the cell. In addition, the data gathered during the development and characterization of the source was used as evidence in support of 4-Wave Mixing model as the mechanism of generation. The thesis will then conclude with the implementation of this new source for multidimensional spectroscopy. Work was spent in the design, layout and the building of a new multidimensional spectroscopy setup that utilize two different mid-IR sources: narrowband IR pulses from the OPA/DFG source and the BBIR source. Preliminary narrowband IR pump-BBIR probe experiments on the deuterated benzoic acid dimer (BA-d_5) and 2D IR experiments on sodium nitroprusside (SNP) were conducted as a test of the setup and the results obtained thus far are similar to those from previous studies [43, 44]. Thus, these experiments demonstrate the viability of this source for the application of multidimensional spectroscopy.

References

[1] Hochstrasser, R. M., *Proc. Natl. Acad. Sci. U. S. A.* **2007,** *104*, 14190-14196.

[2] Kwak, K.; Zheng, J.; Cang, H.; Fayer, M. D., *J. Phys. Chem. B* **2006,** *110*, 19998-20013.

[3] Khalil, M.; Demirdoven, N.; Tokmakoff, A., *J. Phys. Chem. A* **2003,** *107*, 5258-5279.

[4] Piletic, I. R.; Moilanen, D. E.; Levinger, N. E.; Fayer, M. D., *J. Am. Chem. Soc.* **2006,** *128*, 10366-7.

[5] Roberts, S. T.; Ramasesha, K.; Tokmakoff, A., *Acc. Chem. Res.* **2009,** *42*, 1239-49.

[6] Butler, J. M.; George, M. W.; Schoonover, J. R.; Dattelbaum, D. M.; Meyer, T. J., *Coord. Chem. Rev.* **2007,** *251*, 492-514.

[7] Ihalainen, J. A.; Bredenbeck, J.; Pfister, R.; Helbing, J.; Chi, L.; van Stokkum, I. H.; Woolley, G. A.; Hamm, P., *Proc. Natl. Acad. Sci. U. S. A.* **2007,** *104*, 5383-8.

[8] Elliott, A.; Ambrose, E. J., *Nature* **1950,** *165*, 921-922.

[9] Kong, J.; Yu, S., *Acta Biochim. Biophys. Sin* **2007,** *39*, 549-559.

[10] Krimm, S.; Bandekar, J., **1986,** *38*, 181-364.

[11] Susi, H.; Byler, D. M., **1986,** *130*, 290-311.

[12] Venyaminov, S.; Kalnin, N. N., *Biopolymers* **1990,** *30*, 1259-71.

[13] Badger, R. M.; Bauer, S. H., *J. Chem. Phys.* **1937,** *5*, 839.

[14] Buergi, H. B.; Dunitz, J. D., *J. Am. Chem. Soc.* **1987,** *109*, 2924-2926.

[15] Colthup, N. B.; Daly, L. H.; Wiberley, S. E., *Introduction to Infrared and Raman Spectroscopy*. Academic Press: New York, 1990.

[16] Gerwert, K., *Biol. Chem.* **1999,** *380*, 931-5.

[17] von Germar, F.; Barth, A.; Mäntele, W., *Biophys. J.* **2000,** *78*, 1531-1540.

[18] Barth, A.; Zscherp, C., *Q. Rev. Biophys.* **2002,** *35*, 369-430.

[19] Byler, D. M.; Susi, H., *Biopolymers* **1986,** *25*, 469-87.

[20] Hamm, P.; Lim, M.; Hochstrasser, R. M., *J. Phys. Chem. B* **1998,** *102*, 6123-6138.

[21] Chung, H. S.; Ganim, Z.; Jones, K. C.; Tokmakoff, A., *Proc. Natl. Acad. Sci. U. S. A.* **2007,** *104*, 14237-42.

[22] Strasfeld, D. B.; Ling, Y. L.; Gupta, R.; Raleigh, D. P.; Zanni, M. T., *J. Phys. Chem. B* **2009,** *113*, 15679-91.

[23] Baiz, C. R.; Reppert, M.; Tokmakoff, A., *J. Phys. Chem. A* **2013,** *117*, 5955-61.

[24] Kondrashov, D. A.; Roberts, S. A.; Weichsel, A.; Montfort, W. R., *Biochemistry* **2004,** *43*, 13637-13647.

[25] Moncada, S.; Palmer, R. M. J.; Higgs, E. A., *Pharmacol. Rev.* **1991,** *43*, 109-142.

[26] Palmer, R. M.; Ferrige, A. G.; Moncada, S., *Nature* **1987,** *327*, 524-6.

[27] Benabbas, A.; Ye, X.; Kubo, M.; Zhang, Z.; Maes, E. M.; Montfort, W. R.; Champion, P. M., *J. Am. Chem. Soc.* **2010,** *132*, 2811-20.

[28] Swails, J. M.; Meng, Y.; Walker, F. A.; Marti, M. A.; Estrin, D. A.; Roitberg, A. E., *J. Phys. Chem. B* **2009,** *113*, 1192-201.

[29] Kondrashov, D. A.; Montfort, W. R., *J. Phys. Chem. B* **2007,** *111*, 9244-52.

[30] Deflores, L. P.; Ganim, Z.; Nicodemus, R. A.; Tokmakoff, A., *J. Am. Chem. Soc.* **2009,** *131*, 3385-91.

[31] Smith, A. W.; Tokmakoff, A., *Angew Chem Int Ed Engl* **2007,** *46*, 7984-7.

[32] Kim, Y. S.; Hochstrasser, R. M., *J Phys Chem B* **2009,** *113*, 8231-51.

[33] Fayer, M. D., *Annu. Rev. Phys. Chem.* **2009,** *60*, 21-38.

[34] Baiz, C. R.; Kubarych, K. J., *Opt. Lett.* **2011,** *36*, 187-9.

[35] Petersen, P. B.; Tokmakoff, A., *Opt. Lett.* **2010,** *35*, 1962-4.

[36] Cheng, M.; Reynolds, A.; Widgren, H.; Khalil, M., *Opt. Lett.* **2012,** *37*, 1787-9.

[37] Fuji, T.; Suzuki, T., *Opt. Lett.* **2007,** *32*, 3330-3332.

[38] Kim, K. Y.; Taylor, A. J.; Glownia, J. H.; Rodriguez, G., *Nat. Photonics* **2008,** *2*, 605-609.

[39] Roskos, H. G.; Thomson, M. D.; Kreß, M.; Löffler, T., *Laser Photonics Rev.* **2007,** *1*, 349-368.

[40] Théberge, F.; Châteauneuf, M.; Roy, G.; Mathieu, P.; Dubois, J., *Phys. Rev. A* **2010,** *81*, 033821.

[41] Xie, X.; Dai, J.; Zhang, X. C., *Phys. Rev. Lett.* **2006,** *96*, 075005.

[42] Kaindl, R. A.; Wurm, M.; Reimann, K.; Hamm, P.; Weiner, A. M.; Woerner, M., *J. Opt. Soc. Am. B* **2000,** *17*, 2086.

[43] Yamaguchi, S.; Banno, M.; Ohta, K.; Tominaga, K.; Hayashi, T., *Chem. Phys. Lett.* **2008,** *462*, 238-242.

[44] Brookes, J. F.; Slenkamp, K. M.; Lynch, M. S.; Khalil, M., *J. Phys. Chem. A* **2013,** *117*, 6234-43.

Chapter 2

2D IR Spectroscopy of Nitrophorin 4

The work presented in this chapter has been published in the following article:

Cheng, M.; Brookes, J. F.; Montfort, W. R.; and Khalil, M. "The pH-Dependent Picosecond Structural Dynamics in the Distal Pocket of Nitrophorin 4 Investigated by 2D IR Spectroscopy." *J. Phys. Chem. B* **2013.**

Introduction

2.1.1 Introduction

Proteins can be thought of as nature's astounding machinery, in which all the critical parts of this machine are built from a small standard set of only 20 amino acids. Yet, through the numerous combinations of amino acids and the complex folding of the structures, there are many resultant biological cogs and pieces that are essential to life. Hemeproteins are a particular class of proteins in which its function is not only determined by its structure, but also by an additional prosthetic group (or ligand). These ligands are often small molecules, such as oxygen (O_2) or carbon monoxide (CO) that bind to the iron center of the porphyrin complex [1-4]. The resultant functions and dynamics of the protein could drastically change upon binding to a particular ligand. This class of proteins is responsible for a number of biological functions, such as catalysis, electron transport and oxygen transport.

While O_2 binding to hemeproteins is widely studied, there has been an increased interest in nitric oxide (NO) and its interaction with these proteins. NO's importance to various biological processes seems to contradict its notoriety, given that is a reactive molecule (stemming from an unpaired, antibonding electron), has a short half-life in biological systems and is toxic in high concentration [5-8]. Yet, it is known to be a critical component in a number of biological processes such as blood pressure regulation, neurotransmission, immune response and muscle relaxation [9-11].

Nitrophorins (NPs) are a particular class of hemeproteins that bind specifically to NO. These hemeproteins are commonly found in the saliva of blood feeding insects [7, 12].

One of the best characterized nitrophorins is isolated from the salivary gland of the "kissing bug" *Rhodnuis prolixus*. Four out of the seven NPs (NP1-4) function as containers and transporters of NO. NO is stored in the low pH environment of the salivary gland (pH ≈ 5) and is released in the higher pH environment of the host tissue (pH ≈ 7.5). The release of NO into the host serves as a vasodilator while the NPs themselves sequester histamine to enhance the vasodilatory activity and inhibit detection by the host. Thus, given NPs' multifaceted abilities to induce vasodilation and interfere with blood coagulation, additional attention has been given to this protein as it is an ideal model compound for the treatment of cardiovascular diseases [13].

Nitrophorins (1-4) are ~ 20 kDa in size and the pairs NP1/4 and NP2/3 are the most similar in terms of genetic sequence (90% and 79% identical respectively) and function. All four NPs are known to have same structure and fold that is characteristic of the lipocalin protein family. These proteins consist of an eight-stranded β-barrel with a heme at the hydrophobic end. When the heme is not bound to NO, the distal pocket (the active site of the protein, located above the heme) is opened to the solvent and contains several molecules of water.

Upon binding to NO, the protein undergoes several structural changes that dramatically affect the environment of the distal pocket. The first and foremost is the movement of several mobile residues at the mouth of the distal pocket that "lock-in together." At the lower pH ≈ 5 and bound to NO, the protein adopts a "closed" conformation in which the residues collectively characterized as the A-B (residues 31-37) and the G-H (residues 125-132) loops form a network of hydrogen bonds. This consequently shields the distal pocket from the surrounding solvent and hinders NO escape from the protein cavity. Moreover, the movement of the loops results in a more hydrophobic distal pocket by packing hydrophobic residues towards the distal pocket and the expulsion of as many as 3 molecules of water [7]. At the higher pH ≈ 8, the hydrogen bonding network among the loops is disrupted. This "open" conformation with the loops being more mobile and no longer packed into the distal pocket results in a more hydrophillic cavity with the presence of more water. X-ray crystallography studies have shown that these two conformations are found to exist at all pH conditions with an increase of the open conformation at higher pH [9].

Another critical feature of the NP that is crucial to its storage and transport function is the ferric heme itself. The ferric Fe(III) center is ideal for NP since this particular state favors the dissociation of NO and the binding of histamine, whereas the ferrous state is the opposite with irreversible binding to NO and weak association with histamine [13]. Moreover, additional studies have investigated the influence of the non-planar geometry of the heme in stabilizing the ferric charge and the bent bond angle (156°) for Fe(III)-NO [14, 15]. Despite all that is known about the intricate design of the protein, the actual mechanism for NO release and why it is more favorable at the higher pH is not fully understood.

Numerous kinetic studies on the binding and dissociation of NO using histamine and laser photolysis have revealed multi-exponential pH-dependent release rates across a wide range of timescales [16-19]. Mutations made to the two loops (particularly the double mutation D129A/L130A) no longer have pH-dependent release rates, confirming the flexible loops are indeed involved in the pH-dependent protein function [16]. However, the non-exponential and multiphasic release rates of the wild type are still present in the mutant variants, suggesting that other factors are in play with NO release. MD simulations have shown that the opening of the loops resulting in a larger and more solvated distal pocket, along with subtle positional changes to several key residues on the loops are all critical features in governing NO escape into the solvent [8].

Since the loops in the open structure are more mobile, x-ray diffraction studies on the open conformation of NP4-NO often report ambiguous structures with multiple loop positions [17]. Another difficulty in probing the open conformation is the photoreduction of the ferric heme (of the open conformation) due the distal pocket being more solvated [9]. Given that the structural changes within the distal pocket are more subtle than in the loops, in addition to the possible role of water in the solvent reorganization within the distal pocket as another critical element for NO release, another method of studying this protein would be through monitoring the changes of the NO stretching vibration through IR spectroscopy [8, 15, 18].

Besides the hemeprotein itself, there is also a growing body of literature that focuses on the study of ligands. It has been shown that one can use of frequency shifts of the nitrosyl stretching vibration (ν_{NO}) in hemeproteins as a sensitive reporter of the local electric field and Fe-NO bonding interactions [20, 21]. The time-dependent frequency fluctuations of an IR active vibration (δω) are encoded in the frequency-frequency correlation function (FFCF, ⟨δω(t)δω(0)⟩), which is proportional to the first-order (linear) response function ($R^1(t)$). Linear absorption lineshapes can then be obtained through the Fourier transform of the linear response function.

Two-dimensional (2D) IR spectroscopy has been used effectively to measure the FFCF of carbonyl and nitrosyl ligands in hemeproteins to characterize the structural fluctuations around the ligand binding sites [22-30]. The goal of this study is to measure the equilibrium structural dynamics in the distal pocket of NP4–NO as a function of pH. The experiments sample the conformational heterogeneity and directly measure the timescales of equilibrium structural fluctuations in the vicinity of the Fe–NO bond. The extraction of the FFCF for the ν_{NO} and other spectroscopic data obtained will be used to gain further insight into the dynamic distal pocket environment and the non-exponential NO release rates in NP4-NO.

Methods

2.2.1 Sample Preparation

Nitrophorin 4 was overexpressed from an *Escherichia coli* strain and refolded from inclusion bodies supplemented with heme, as described in reference [31]. In order to resolve the weak mid-IR absorption band of the NO stretching vibration at ~ 1905 cm^{-1} from the absorbance of H_2O in the same spectral region, samples of purified ferric NP4 underwent a buffer exchange process to replace the 20 mM sodium phosphate buffer (at pH 7.0) with a deuterated buffer. Acidic (pD 5.1) and basic (pD 7.9) 20 mM potassium dideuterium phosphate (KD_2PO_4) buffer solutions were prepared in D_2O. Centrifugal filter devices (Amicon Ultra-0.5) were used to exchange the aqueous buffer as well as to concentrate the protein samples. In order to prepare the ferric NP4–NO complex, fresh NO gas was generated by mixing ascorbic acid (880 mg in 25 mL of water) and sodium nitrite (40-60 mg) after degassing each of them under Ar for at least 30 minutes. The sample was also degassed for at least 15 minutes prior to flushing with the generated NO gas using an airtight syringe.

Linear FTIR (Jasco FT/IR-4100) and UV-Vis (Jasco V-630) spectra of the samples were obtained (sample path length = 50 μm) before and after each 2D IR scan to ensure that the protein had not degraded during the experiment. The final concentrations of the protein sample at the start of each scan were determined by the intensity of the alpha and beta bands in the UV-Vis spectra of ferric NP4-NO [15]. The final concentrations were 4.1 mM and 6.4 mM for the acidic and basic sample respectively. These concentrations yield an OD of 0.037 and 0.046 for the ν_{NO} peak at 1905 cm^{-1}.

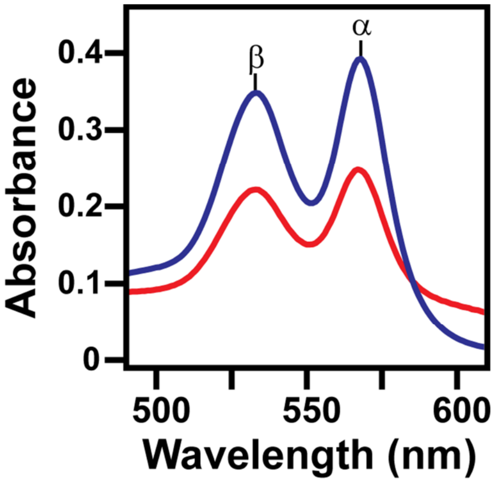

Figure 2.1. UV-Vis spectra of ferric NP4-NO at pD 5.1 (red) and pD 7.9 (blue). The concentration of the samples were determined by the measured absorbance of the α and β bands that appear at 568 nm and 532 nm. The extinction coefficient the α and β bands are 11 and 12 mM^{-1} cm^{-1} [15].

2.2.2 2D IR Experiment

Femtosecond pulses of mid-IR light were generated from a combination of commercial equipment, beginning with a regenerative amplifier (Spectra Physics Spitfire Pro-35F-XP), which outputs 3 W, 800 nm, 35 fs pulses of light at 1 kHz. Approximately 1 W of the 800 nm output is sent to an optical parametric amplifier (OPA-800C) to produce the near-IR signal and idler pulses. The two near IR fields undergo difference frequency mixing in a 0.5 mm $AgGaS_2$ crystal to generate 80fs mid-IR pulses with a spectral bandwidth of ~200 cm^{-1} at a center wavelength of 5.1 μm.

Each single mid-IR pulse generated by the OPA/DFG source is then sent into a five-beam interferometer to generate three input pulses, a tracer beam and a local oscillator field as described in Ref [32, 33]. The three input IR beams have parallel polarizations and are arranged in the boxcar geometry, temporally overlapped, and focused onto the sample with a spot-size of ~150 μm. Each of the input beams has ~0.2 μJ of energy per pulse. The home-built sample cell is equipped with two 1 mm CaF_2 windows and a 50 μm Teflon spacer. The resulting background-free signal field is overlapped with the local oscillator field on a beamsplitter for heterodyne detection. The reflected and transmitted combined signal and local oscillator fields are π out of phase with respect to each other and are detected at the focal plane of a spectrometer (Triax 190, Horiba Jobin Yvon, 150 1ines/mm grating) using a 2 × 64 mercury cadmium telluride (MCT) array detector (IR0144, Infrared Systems Development). We subtract signals from the two linear MCT arrays to perform "balanced detection" on a shot-to-shot basis as explained in Ref [32].

The evolution (τ_1) and waiting (τ_2) time delays between the consecutive pairs of pulses 1, 2 and 2, 3 were accurately controlled by Newport XMS50 linear stages. Rephasing and non-rephasing experiments were performed at each τ_2 delay in order to construct absorptive 2D IR correlation spectra. The τ_1 delay was scanned in 4 fs steps from 0 to 4 ps for the rephasing experiments and from 0 to 3 ps for the non-rephasing experiments. The τ_2 delay was scanned in unequal time steps from 0 to 70 ps and each data point is comprised of an averaged collection of 2000 laser shots. The raw experimental data was zero padded to 32.8 ps and Fourier transformed along τ_1 to obtain the ω_1 axis. The final 2D IR spectrum is corrected for the phase ambiguities corresponding to drift of the relative timing between the local oscillator and signal fields by comparing the projection of the 2D IR spectrum along the ω_1 axis to a two-beam dispersed pump-probe spectrum collected for the same values of τ_2.

Results

2.3.1 pD Dependent FTIR Spectra

The background subtracted linear FTIR spectra of the ligated protein at each pD are shown together in figure 2.2. The dashed lines in the figure represent the Gaussian fits to the spectra for each pD and listed in table 2.1 are the results of the best fits using two Gaussian functions. The peak centered at ~1905 cm^{-1} represents the closed conformation while the other peak at ~1917 cm^{-1} represents the open conformation that has the mobile loops and hydrophobic distal pocket [17, 18, 34]. For simplicity, the peak at ~1905 cm^{-1} is labeled as A_0 and the peak at ~1917 cm^{-1} is labeled as A_1. Although the two conformations are present at both pDs, there is a greater percentage of the open conformation present at the higher pD. The ratio of the area under the Gaussian curves (AUC) corresponding to the open and the closed conformation was 0.19 at pD 5.1 and 0.34 at pD 7.9.

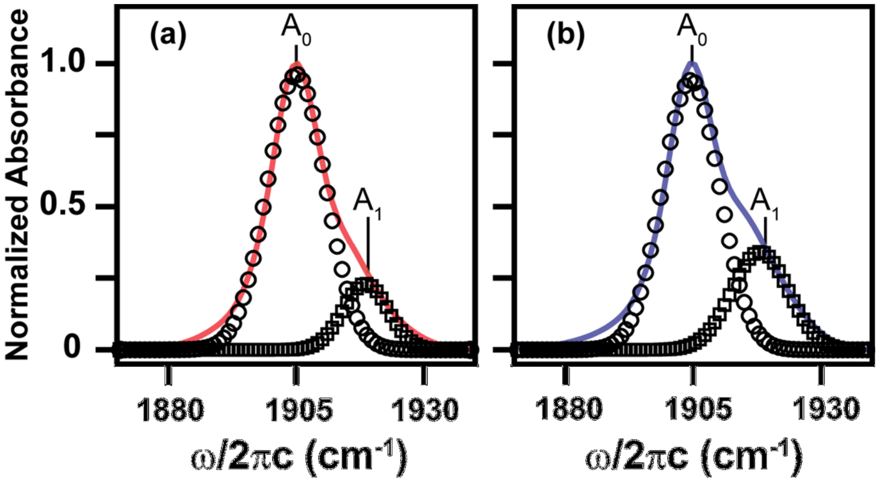

Figure 2.2. The linear FTIR spectra (solid line) of the ferric NP4-NO protein in an acidic (a) and basic (b) buffer. The circle and square dots are the two Gaussians curves used in the fit the peaks A_0 and A_1 respectively. These peaks correspond to the closed conformation (A_0) and the open conformation (A_1).

	$\mathbf{A_0}$			$\mathbf{A_1}$			$\mathbf{A_0/A_1}$
	Center (cm^{-1})	**Width (cm^{-1})**	**Amp**	**Center (cm^{-1})**	**Width (cm^{-1})**	**Amp**	**Ratio AUC**
pD 5.1	1905.09	13.36	0.96	1918.58	10.36	0.23	0.19
pD 7.9	1904.55	13.16	0.94	1918.04	13.06	0.34	0.36

Table 2.1. Summary of the parameters obtained from the Gaussian fits to the linear FTIR spectra.

The presence of two conformational substates of NP4-NO (A_0 and A_1) in the FTIR spectra at each pD coincides with previous high-resolution crystal structures of hemeprotein at pH 5.6 and 7.5 [9]. The distal pocket configuration for the closed and open conformational sub-states of NP4-NO at both pH conditions are shown collectively in figure 2.3.

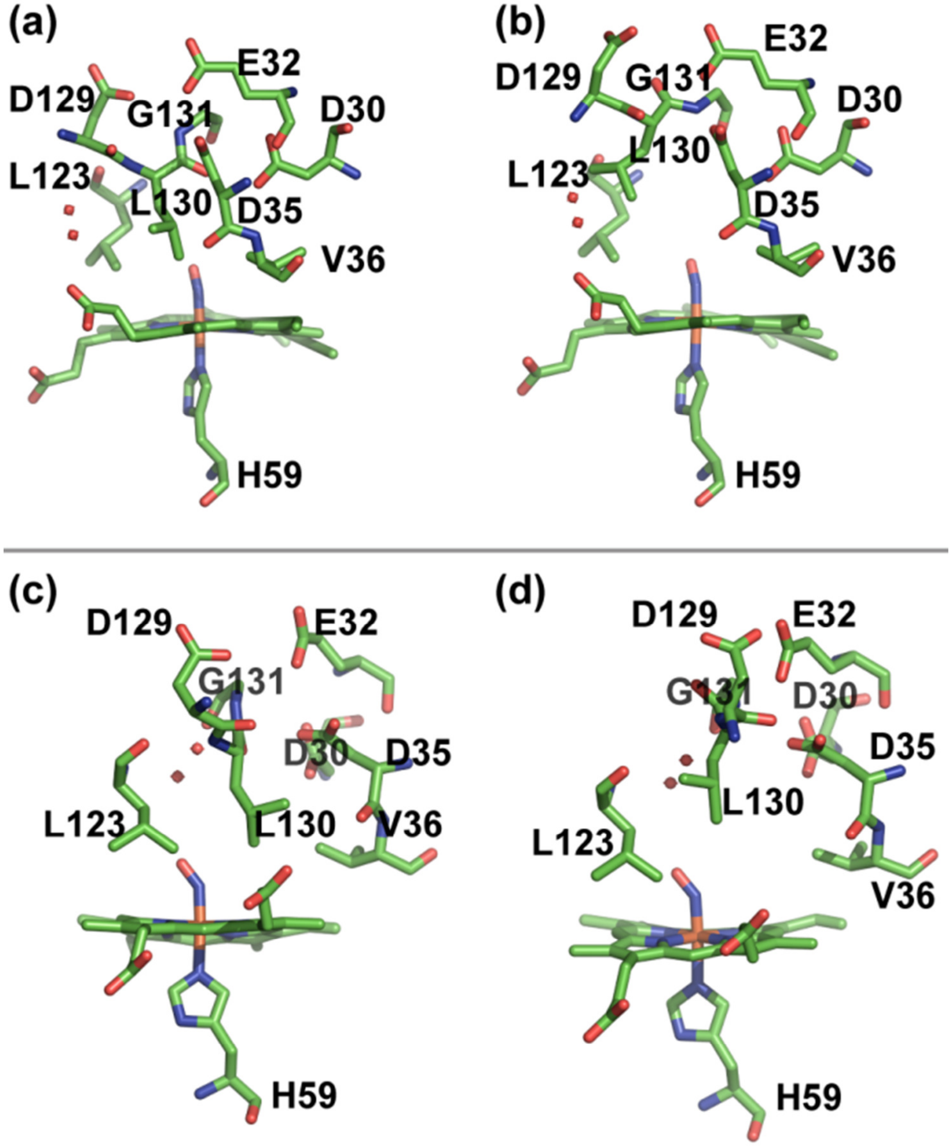

Figure 2.3. Multiple conformers of NP4-NO determined by X-ray crystallography. The top panel shows the closed (a) and open (b) conformers at pH 5.6 (PDB ID 1X8O). The bottom panel shows the closed (c) and open (d) conformers at pH 7.5 (PDB ID 1X8N).

One of the primary differences amongst the different configurations is the structural order of the A-B loops. This loop is most ordered for the closed conformation at pH 5.6 (figure 2.3a) due to the numerous hydrogen bond interactions between the residues on the A-B and G-H loops. However, this hydrogen bonding network is severely disrupted at the higher pH due to the deprotonation of those key residues involved [9, 18]. Crystal structures of NP4-NH_3 (representative of the open conformer) and the NP4-NO (closed conformer) have also shown that the loop is more disordered for each conformer at high pH than their respective counterpart at low pH [9]. As such, the four distal pocket configurations can be differentiated by the ordering of A-B loop as follows: (2.3a) closed conformation at pH 5.6 (most ordered) > (2.3b) open conformation at pH 5.6 > (2.3c) closed conformation at pH 7.5 > (2.3d) open conformation at pH 7.5 (least ordered).

Another difference amongst the distal pocket configurations is the position of Leu 130 on the G-H loop. Unlike the A-B loop, the G-H loop has two fixed conformations: one associated with the closed conformation, in which the Leu 130 points towards the distal pocket and is packed against the ligand. The other is associated with the open conformation, which has the Leu 130 moved away from the pocket.

The different combination of these structural changes in the loops has numerous effects on the distal pocket environment. The result of the loop closure not only creates a physical barrier between the distal pocket and the solvent but also packs non-polar side chains tightly around the NO ligand. Along with the packing of the nonpolar residue Leu 130 against the ligand as well, the distal pocket environment of the closed conformation at pH 5.6 is highly nonpolar and hydrophobic [8, 9, 15, 16]. For the open conformation at pH 7.5, the physical barrier is broken with the disruption of the hydrogen bonding network between the loops. Moreover, the movement of the Leu 130 away from the distal pocket provides additional space for the solvent molecules that can now permeate pass the loops and occupy the pocket. The position of the electron density of Leu 130 in the open conformer matches closely with the NP4-NH_3 crystal structure at pH 7.4 which shows the presence of as many as ~5 water molecules in the distal pocket.

2.3.2 pD Dependent 2D IR Spectra

Although the peaks corresponding to the two conformations have been identified, the timescales and nature of the underlying structural fluctuations that give rise to the FTIR linewidths are unknown. Using 2D IR spectroscopy, the dynamic structural information can be obtained by monitoring the evolution of the lineshapes as a function of τ_2. At early τ_2 times, the 2D peaks are characteristically elongated along the diagonal axis as a result of inhomogeneous broadening (representing a distribution of structures). As τ_2 evolves, spectral diffusion causes the vibrational frequencies between the two experimental time periods (τ_1 and τ_3) to lose correlation, resulting in more symmetric 2D lineshapes. A set of absorptive 2D IR spectra, ranging from $\tau_2 = 0$ ps → 80 ps, were obtained for the ligated protein at each pD. Shown in the figures 2.4 and 2.5 are a selection of absorptive 2D IR spectra of the ligated protein at the indicated τ_2 delays at pD 5.1 and 7.9.

In each of the spectra, there are positive and negative peaks that correspond to the $\nu_{NO}^{0\rightarrow1}$and the $\nu_{NO}^{1\rightarrow2}$ vibrational transitions of the NO ligand. The separation of the two peaks is a direct measure of the vibrational anharmonicity of the ν_{NO} in NP4-NO. Since the intensity of the A_1 peak at pD 5.1 was weak, it was excluded from most of the subsequent analysis that follows. For all other peaks that can be observed, the vibrational anharmonicity was determined to be 29±2 cm^{-1} for the A_0 at both pD. The same value (within error) was also observed for the A_1 feature at pD 7.9. This value is similar to previously reported vibrational anharmonicity of the ν_{NO} in other hemeproteins [22, 26-28].

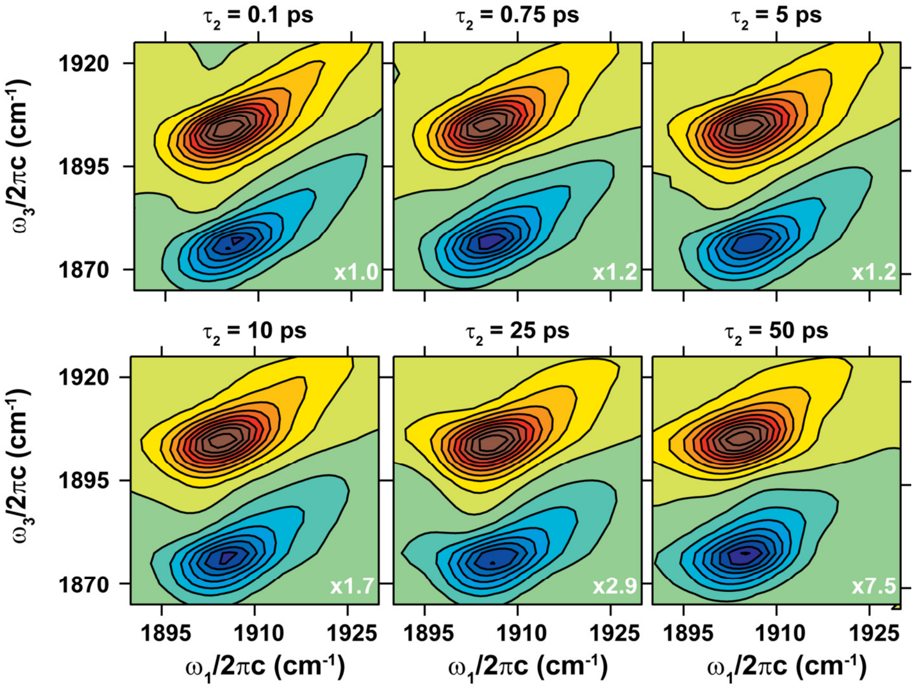

Figure 2.4 Experimental 2D IR spectra of ν_{NO} in NP4-NO at pD 5.1. Contour levels are drawn at 10% intervals.

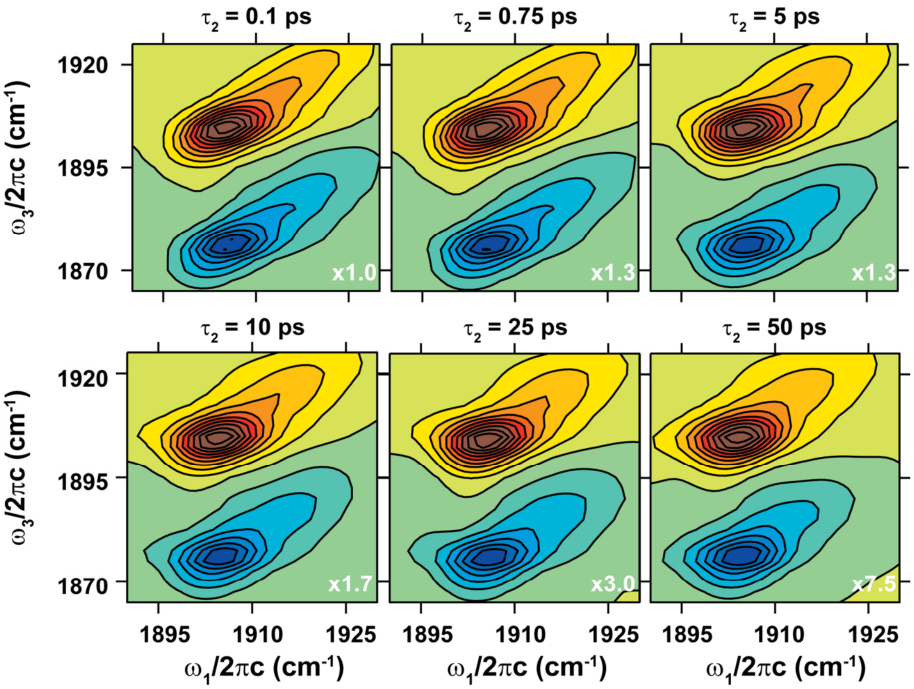

Figure 2.5. Experimental 2D IR spectra of ν_{NO} in NP4-NO at pD 7.9 Contour levels are drawn at 10% intervals.

The evolving 2D lineshape is a direct measure of the FFCF and yields information on the timescales and amplitudes of the structural fluctuations for the closed and open conformations of NP4-NO. The center line slope method (CLS) outlined in Ref [35] was used to extract the FFCF from the positive peaks of the spectra. The CLS method entails taking a slice along ω_1, resulting in a 1D spectrum with only the ω_3 axis. From this, one looks for the value of ω_3 corresponding to the point of highest spectral amplitude. This is repeated for a number of ω_1 slices resulting in a number of $[\omega_1,\omega_3]$ coordinates (the points are indicated in figures 2.6 as either circles or squares). A line is fitted through these points and a value for the slope of the center line is obtained. A value of 1 for the CLS corresponds to the inhomogeneous limit and appears in the spectra as completely elongated 2D lineshape along the diagonal. On the other hand, a value of zero for the CLS corresponds to the homogenous limit, in which the peak is completely symmetric as spectral diffusion has sampled all possible frequencies within the distribution.

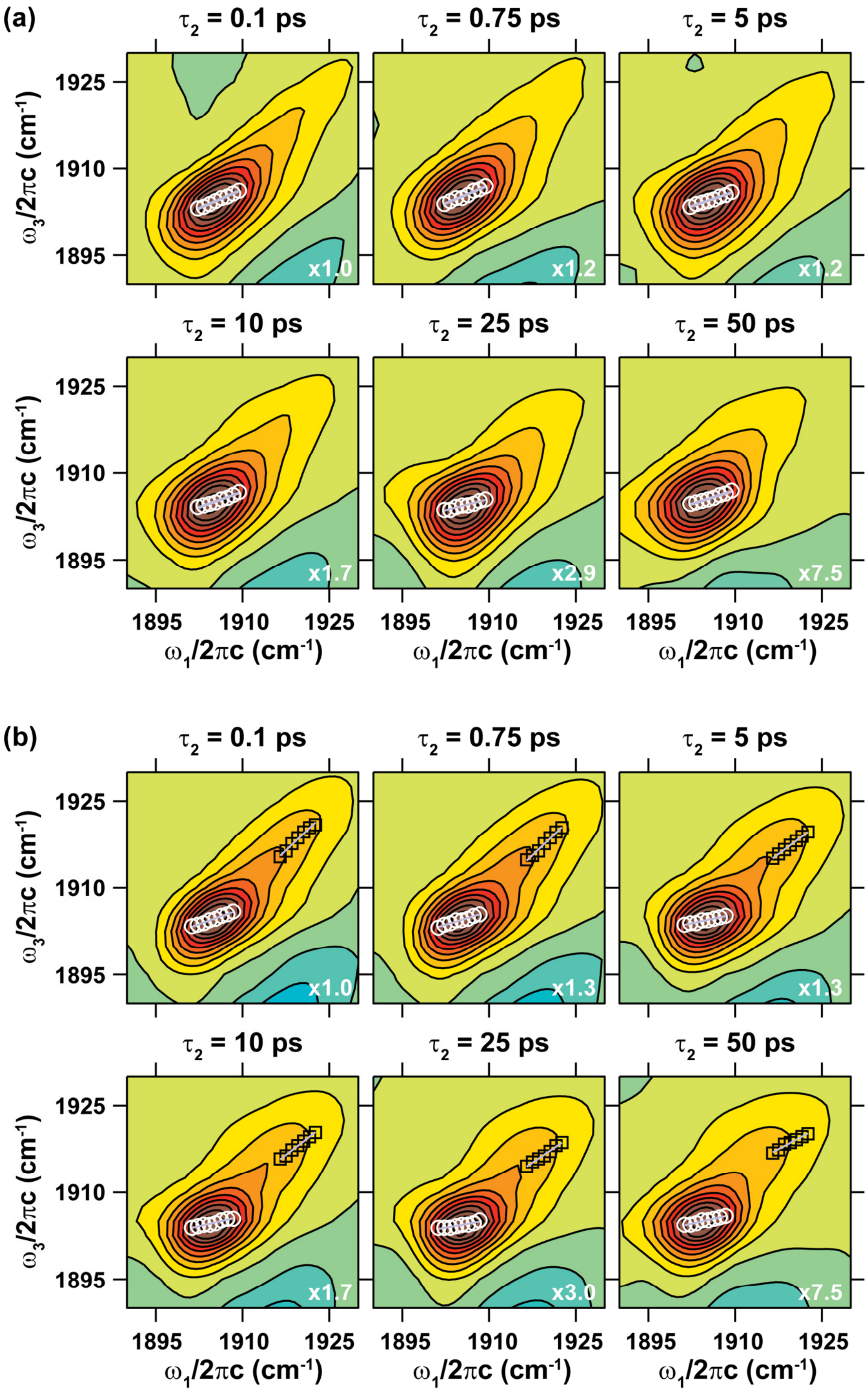

Figure 2.6. The absorptive correlation spectra for ferric NP4-NO at (a) pD 5.1 and (b) pD 7.9 as a function of τ_2. The white circles and the black boxes represent the points used in the fits for A_0 and A_1 respectively. A line was fitted to these sets of points in order to extract the center line slope (indicated by the gray lines through the points).

From the CLS analysis, values of the slope were obtained for the 2D IR spectra collected at each τ_2 and the collective data is plotted in figure 2.7. The CLS (as a function of τ_2) is proportional to the FFCF and the data was fitted to the FFCF of the following form:

$$C(t) = \sum_{i=1}^{2} \Delta_i^2 \, exp\left(-\frac{t}{\tau_{ci}}\right)$$

where τ_{ci} refers to the timescale of the frequency fluctuations for the particular ν_{NO} peak with an amplitude Δ_i. The values for the timescales and amplitudes obtained from the CLS analysis were then used to simulate the linear FTIR spectra. The FFCF was used to obtain the line shape function:

$$g(t) = \int_0^t d\tau_2 \int_0^{\tau_2} d\tau_1 \, C(\tau_1)$$

which can then be used to obtain linear response function ($R^1(t)$):

$$R^1(t) = \left|\mu_{0,1}\right|^2 e^{-i\langle\omega_{0,1}\rangle t} \exp[-g(t)] \exp(-t/T_2)$$

where $1/T_2 = 1/T_2^* + 1/2T_{vib,lif}$. The Fourier transform of the linear response function then yields the linear absorption spectra as shown in the insert of figure 2.7.

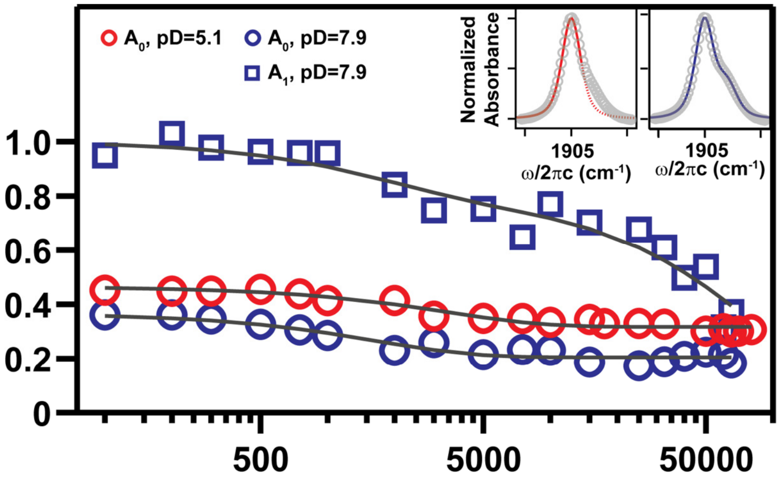

Figure 2.7. CLS decays for the ν_{NO} in NP4–NO at pD 5.1 and 7.9. The insets show fits (solid) of the FTIR spectra (circles) based on the measured CLS decays

Values of the amplitudes were floated in an iterative process until the simulated linear FTIR was in agreement with the actual spectra. The values obtained from the iterative linear FTIR fit are listed in table 2.2. This procedure allowed us to obtain the homogenous linewidth (π/T_2^*) for each of the protein confirmations. The vibrational lifetime ($T_{vib,lif}$) of the first excited state of ν_{NO} for both sub-populations of NP4-NO was measured with IR pump-probe experiments and was determined to be 30 ps.

	Δ_1 (ps^{-1})	**τ_{c1} (ps)**	**Δ_2 (ps^{-1})**	**τ_{c2} (ps)**	**T_2^* (ps)**
pD 5.1					
A_0	0.46 ± 0.01	4 ± 1	0.67 ± 0.01	∞	2.11 ± 0.03
pD 7.9					
A_0	0.48 ± 0.01	1.7 ± 0.8	0.54 ± 0.01	∞	2.03 ± 0.05
A_1	0.65 ± 0.02	1.3 ± 0.8	1.3 ± 0.1	100 ± 30	∞

Table 2.2. Parameters of the FFCF of the ν_{NO} at pD 5.1 and 7.9 after the iterative fitting routine to the FTIR spectra.

Final values for the timescales, the amplitude and the homogenous linewidths were obtained through an additional spectral fitting routine that was done later by the group and published in Ref [36]. Using the values listed in table 2.2 as the initial starting values, this additional procedure involves the iteratively fitting of the simulated 2D spectra with the obtained spectra collected at each τ_2. Fits with this routine accounted for additional parameters such as the vibrational anharmonicity ($\Delta_{12} = 2\nu_{\mathrm{NO}}^{0\to1} - \nu_{\mathrm{NO}}^{0\to2}$) and changes in the 2D lineshapes as a function of τ_2, for both the $\nu_{\mathrm{NO}}^{0\to1}$and the $\nu_{\mathrm{NO}}^{1\to2}$ vibrational transitions of NP4-NO. This not only provided more accurate values for the parameters of the FFCF, but it also allowed the extraction of such information for the open conformation at pD 5.1 (the weak shoulder A_1). The best-fit values of this procedure are listed in table 2.3 and the subsequent discussion is based on these results.

	Δ_1 (ps^{-1})	τ_{c1} (ps)	Δ_2 (ps^{-1})	τ_{c2} (ps)	T_2^* (ps)	Δ_{12} (cm^{-1})
pD 5.1						
A_0	0.55 ± 0.04	3 ± 1	0.57 ± 0.57	∞	7 ± 2	30 ± 2
A_1	0.40 ± 0.06	0.9 ± 0.4	1.4 ± 0.1	130 ± 0.30	7 ± 2	29 ± 2
pD 7.9						
A_0	0.3 ± 0.1	1.4 ± 0.7	0.36 ± 0.04	∞	7 ± 2	30 ± 2
A_1	0.57 ± 0.07	0.8 ± 0.4	1.2 ± 0.1	70 ± 30	7 ± 2	29 ± 2

Table 2.3. Best fit parameters of the FFCF for the ν_{NO} in NP4-NO extracted from fitting the 2D IR data.

Discussion and Conclusion

2.4.1 pD-Dependent 2D IR Spectra and Extraction of the FFCF Parameters

The final values for the timescales and amplitudes of the structural fluctuations for both the A_0 and A_1 peaks of NP4-NO at each pD are listed in table 2.3. The homogenous contribution to the IR linewidth is governed by the protein and solvent fluctuations much faster than the experimental time resolution of this 2D IR experiment. From the analysis, the homogenous dephasing time (T_2^*) for the A_0 and A_1 peaks of the υ_{NO} are the same. This is also true regardless of pD since T_2^* was determined to be universally 7 ps. However, the timescales of the structural fluctuations are very different between the two peaks. Each peak exhibited a fast and a slow (τ_{c1} and τ_{c2}) timescales which also differed with pD.

The strong positive 2D peaks in the spectra shown (figures 2.4-2.6) are elongated along the diagonal axes at early τ_2. The elongation of the diagonal peak represent a distribution of structures for both the closed (A_0) and open (A_1) conformations of NP4-NO. As τ_2 increases, structural fluctuations would cause the vibrational frequencies to lose correlation (spectral diffusion) and consequently causing the 2D lineshapes to become more symmetric. In this set of 2D IR spectra, the A_0 peak remains elongated for the entirety of the experimental window (for as long as τ_2= 80 ps). A qualitative comparison between the A_0 and A_1 peaks at τ_2= 50 ps suggests that the latter peak undergoes faster frequency fluctuations.

At pD 5.1, the ν_{NO} of the closed conformer exhibits fast structural fluctuation on a 3 ps timescale (τ_{c1}) while a significant portion of the dynamics are too slow to be measured within the experimental time window of ~100 ps. As a result, the timescale of the slow fluctuation is listed as $\tau_{c2}=\infty$ in table 2.3. However, the ν_{NO} of the open conformer exhibits measurable fast (τ_{c1}) and slow (τ_{c2}) structural fluctuations on a 0.9 ps and a 130 ps timescale. Simiarly, for the dynamics of NP4-NO at pD 7.9, the υ_{NO} of the closed conformer exhibits slow fluctuation that exceed the experimental time window of ~100 ps ($\tau_{c2}=\infty$) while the fast structural fluctuation occurs on a 1.4 ps timescale. The υ_{NO} of the open conformer exhibits measurable fast and slow structural fluctuations on a 0.8 ps and a 70 ps timescale respectively.

The fast (τ_{c1}) frequency fluctuation of the A_0 and A_1 peaks at each pD were assigned to fluctuations of the local electric field around the nitrosyl ligand in NP4-NO. Previous work on the characterization of the FFCF of the ν_{NO} in sodium nitroprusside (SNP) revealed a negative correlation between the solvent polarity and the timescale for spectral diffusion [33]. The solvent polarity was defined by the empirical solvent parameters: $E_T^N(30)$ and the acceptor number (AN) [37]. The measured τ_{c1} values of ν_{NO} of SNP (in order of increasing solvent polarity) were: ethanol (3.8 ps), methanol (2.3 ps), D_2O (1.4 ps) and H_2O (0.84 ps). The results from this 2D IR experiment confirms previous studies that indicate the distal pocket environment surrounding the ligand in the open conformation is more polar than the closed conformation. Moreover, crystal structures have also reported an increase in the polarity of the distal pocket upon an increase in pH. This change as a function of pH is reflected in the 2D IR data as the timescale for spectral diffusion of the closed conformer decreased from 3 ps (at pD 5.1) to 1.4 ps (at pD 7.9).

The slow (τ_{c2}) frequency fluctuation of the A_0 and A_1 peaks at each pD were assigned to the structural dynamics of the loop regions of NP4-NO. The slow frequency fluctuations of the ν_{NO} in the closed conformer (regardless of pD) were too slow to be measured on the timescale of the experiment and appears as static. However, values for τ_{c2} of the open conformer were measurable and undergoes frequency fluctuations on the 130 ps and 70 ps timescale for the pD 5.1 and 7.9 respectively. The findings here are consistent with X-ray crystallography studies, which have shown that the A-B and G-H loops are poorly modeled for the open conformers of the NP4-NO protein [9]. Although the

A-B and G-H loops are still mobile for closed conformations, it is more “rigid” in comparison to the open conformation. Hence, the dynamics appear to be frozen for these conformers on the 100 ps timescale.

2.4.2 Relating Structure, Function and Dynamics in NP4

The results of the 2D IR lineshape analysis reveal a picture of a dynamic distal pocket with structural fluctuations on a range of timescales. The timescales and amplitudes on the equilibrium structural fluctuations support the existing body of work that has been done to unravel the mechanism of NO transport and release. The fact that there is no simple explanation of this mechanism reflects the intricate design and the complex interplay of the various components of the protein that work in harmony. Some of the physical characteristics critical to function are: the distal pocket environment, the mobility of the loops, the charge of the heme center and the non-planarity of the heme.

The binding and release of NO from the heme has been described as the following two step process [15]:

$$\text{NP-NO} \underset{k_{on}}{\overset{k_{off1}/k_{off2}\,\text{(pH dep.)}}{\rightleftarrows}} [\text{NP:NO}] \underset{k_{-1}}{\overset{k_{1}}{\rightleftarrows}} \text{NP} + \text{NO}$$

In this model, NO dissociation occurs with two pH-dependent rates ($k_{off1,2}$) involving a slow protein conformational change followed by a faster rate (k_1) representing the escape of NO into the solvent from the distal pocket of the complete open conformation [16]. While the slower off-rates do not represent the interconversion between the close and open conformers (which occurs on timescales of nanoseconds and > 100 s at 200 K), these slower off-rates are attributed to the mobile A-B and G-H loop regions [16-18, 38]. Kinetic experiments on NP4 mutants with changes to key residues that are critical to loop closure resulted in measured kinetic rates that were no longer a function of pH. However, these rates remained biphasic.

It has been postulated that existence of the biphasic release rate is the result of different interactions of the NO and its local environment. One study suggests that the biphasic nature might reflect the presence of an internal minipocket within the distal pocket that is more restrictive for NO escape than from the general cavity [38]. At the moment, results from this 2D IR study only confirms that there is indeed a static distribution of the closed conformers at both pH conditions and a distribution of interconverting open conformers on the ~100 ps timescale.

The difference in the timescales of the fast fluctuation (τ_{c1}) as a function of pD support previous studies that reported the presence of additional molecules of water and its close proximity to the iron heme center at the higher pH. X-ray crystal structures have revealed many as 5 molecules of water within the distal pocket and MD simulations have shown that the average Fe-O_{water} distance is approximate 5 Å [8]. At the lower pH, there is only one molecule of water in the distal pocket and the average Fe-O_{water} distance is approximate 7 Å. The abundance and proximity water plays a critical role in NO release by preventing the geminate rebinding between the ligand and heme. The blockage of the iron heme center (by water) facilitates NO escape from the protein matrix into the solvent. Moreover, the closure of the loops due to a network of hydrogen bonds (representative of the static τ_{c2} timescales) results in a smaller, desolvated and well-organized distal pocket. As a result, the slower τ_{c1} timescales of the open conformation reflects the restricted motion of the ligand within the pocket that permits a favorable orientation for rebinding [8, 18].

In addition to its effect on the distal pocket environment, the mobility of the loops have an additional role in the NO release mechanism. MD simulations have shown that positional fluctuations of key residues of the loops are greater for the open conformation and at higher pH [8, 38]. Each of these changes not only opens the loops, but also creates a pathway at the end of the heme barrel that is wide enough for the ligand to escape [8]. The mobility of the loops is reflected in this 2D IR study by the timescales of the slow fluctuation (τ_{c2}) that were measured. The static timescales reflect the "rigidity" of the closed conformations (at both pD) and the decreases of τ_{c2} timescales for the open conformer from 130 to 70 ps (from pD of 5.1 to 7.9) reflects the destabilization of the loops as a function of pH.

The results of this study has provided experimental verification for MD simulations which have suggested that the structural loops in NP4 should not be viewed as rigid cages that confine NO, but rather as a "dynamical oil droplet" that contains NO within the fluctuating nonpolar pocket [8, 9]. While the tight binding of the "oily" (non-polar) side chains in the distal pocket (of the closed conformation) do fluctuate, it does not provide a passage wide enough for the NO diffusion into the solvent and consequently encourages geminate rebinding at the low pH environment. Timescales of 3 ps and ~1 ps that were measured for fast structural fluctuations reflect the hydrophobic and hydrophilic character of the distal pocket.

Future

2.5.1 Future

There are many paths in which the future direction of this work can take. One will be to perform 2D IR studies on mutant variants of NP4 that have changes to residues on the A-B and G-H loops. Mutations to the Asp 30 in particular not only affect the binding and release rates of NO but result in rates that no longer have pH dependence. However, the release rates remain biphasic which suggest that (to some degree) the heterogeneous nature of the distal pocket is pH independent. Thus, measuring the FFCF of the ν_{NO} in these mutants will provide additional insight focused solely on the equilibrium structural fluctuations in the distal cavity and how it relates to the function of this NO storage/transporter protein.

Another future direction will be to do comparative 2D IR studies, such as between NP4 and NP2. Although both NPs share the same eight-stranded β-barrel structure, there are subtle differences between the two that result in drastic differences in the binding rates (10-22 times larger for NP2) and release rates (2-12 folds smaller for NP2) [13]. A key difference between NP4 and NP2 is within the distal pocket, where the Thr 121 of NP4 (which hydrogen bonds to water molecules in the open conformation) is replaced with a nonpolar Ile 120. This increase of nonpolar and hydrophobic character of the NP2 distal pocket not only results in a greater ordering of the distal pocket but also causes the loops to be packed tighter as well. MD simulations have shown that the conformational changes (mainly of the loops) in NP2 differ by no more than 3 Å while those of NP4 differ as much as 8 Å.

Another informative comparative study would between NP4 and ferric myoglobin. The rates of NO binding/release to ferric myoglobin are 10/2000 faster than those for NP4, in addition to being described by a single phase [39]. A recent study has measured the

FFCF of the ν_{NO} in wild-type ferric myoglobin-NO to have a timescale of 3 ps and significant portions of the dynamics were too slow to measure on the experimental timescale [22]. In comparison with the NP4-NO 2D IR results presented, the ν_{NO} in wild-type ferric myoglobin-NO lacks equilibrium structural fluctuations on the 70-100 ps timescale. This suggests that the equilibrium frequency fluctuations arising from local electric field fluctuations in the distal pocket and the loop dynamics have a role to play in regulating the uptake and diffusion of the nitrosyl ligand in NP4.

Furthermore, the structures of nitrophorin and myoglobin are drastically different. While nitrophorins are comprised of β-sheets, myglobin is comprised of α-helices. It has been suggested that the difference in the underlying mechanism of NO release between the two proteins is the result of "inherent dynamic properties" of the secondary structure [38]. Therefore, it might be instructive to do 2D IR studies that the simultaneous monitor the local structural fluctuations (around ν_{NO}) and the global structural fluctuations (by probing the numerous ν_{amide} vibrations) [40-42]. The use of a spectral broadband IR probe would permit such study and may reveal correlations between the local and global secondary structural fluctuations [43-45].

References

[1] Kundu, S.; Trent, J. T.; Hargrove, M. S., *Trends Plant Sci.* **2003,** *8*, 387-393.

[2] Marti, M. A.; Crespo, A.; Capece, L.; Boechi, L.; Bikiel, D. E.; Scherlis, D. A.; Estrin, D. A., *J. Inorg. Biochem.* **2006,** *100*, 761-70.

[3] Simonneaux, G.; Bondon, A., *Chem. Rev.* **2005,** *105*, 2627-46.

[4] Jain, R.; Chan, M. K., *J. Biol. Inorg. Chem.* **2003,** *8*, 1-11.

[5] Laverman, L. E.; Ford, P. C., *J. Am. Chem. Soc.* **2001,** *123*, 11614-11622.

[6] Ford, P. C.; Fernandez, B. O.; Lim, M. D., *Chem. Rev.* **2005,** *105*, 2439-55.

[7] Montfort, W. R.; Weichsel, A.; Andersen, J. F., *Biochim. Biophys. Acta* **2000,** *1482*, 110-8.

[8] Swails, J. M.; Meng, Y.; Walker, F. A.; Marti, M. A.; Estrin, D. A.; Roitberg, A. E., *J. Phys. Chem. B* **2009,** *113*, 1192-201.

[9] Kondrashov, D. A.; Roberts, S. A.; Weichsel, A.; Montfort, W. R., *Biochemistry* **2004,** *43*, 13637-13647.

[10] Moncada, S.; Palmer, R. M. J.; Higgs, E. A., *Pharmacol. Rev.* **1991,** *43*, 109-142.

[11] Palmer, R. M.; Ferrige, A. G.; Moncada, S., *Nature* **1987,** *327*, 524-6.

[12] Lavoipierre, M. M. J.; Kickerson, G.; Gordon, R. M., *Ann. Trop. Med. Parasitol.* **1959,** *53*, 15.

[13] Andersen, J. F.; Ding, X. D.; Balfour, C.; Shokhireva, T. K.; Champagne, D. E.; Walker, F. A.; Montfort, W. R., *Biochemistry* **2000,** *39*, 10118-10131.

[14] Roberts, S. A.; Weichsel, A.; Qiu, Y.; Shelnutt, J. A.; Walker, F. A.; Montfort, W. R., *Biochemistry* **2001,** *40*, 11327-11337.

[15] Maes, E. M.; Roberts, S. A.; Weichsel, A.; Montfort, W. R., *Biochemistry* **2005,** *44*, 12690-9.

[16] Maes, E. M.; Weichsel, A.; Andersen, J. F.; Shepley, D.; Montfort, W. R., *Biochemistry* **2004,** *43*, 6679-90.

[17] Nienhaus, K.; Maes, E. M.; Weichsel, A.; Montfort, W. R.; Nienhaus, G. U., *J. Biol. Chem.* **2004,** *279*, 39401-7.

[18] Benabbas, A.; Ye, X.; Kubo, M.; Zhang, Z.; Maes, E. M.; Montfort, W. R.; Champion, P. M., *J. Am. Chem. Soc.* **2010,** *132*, 2811-20.

[19] Abbruzzetti, S.; He, C.; Ogata, H.; Bruno, S.; Viappiani, C.; Knipp, M., *J. Am. Chem. Soc.* **2012,** *134*, 9986-98.

[20] Soldatova, A. V.; Ibrahim, M.; Olson, J. S.; Czernuszewicz, R. S.; Spiro, T. G., *J. Am. Chem. Soc.* **2010,** *132*, 4614-25.

[21] Spiro, T. G.; Soldatova, A. V.; Balakrishnan, G., *Coord. Chem. Rev.* **2013,** *257*, 511-527.

[22] Adamczyk, K.; Candelaresi, M.; Kania, R.; Robb, K.; Bellota-Anton, C.; Greetham, G. M.; Pollard, M. R.; Towrie, M.; Parker, A. W.; Hoskisson, P. A.; Tucker, N. P.; Hunt, N. T., *Phys. Chem. Chem. Phys.* **2012,** *14*, 7411-9.

[23] Bagchi, S.; Nebgen, B. T.; Loring, R. F.; Fayer, M. D., *J. Am. Chem. Soc.* **2010,** *132*, 18367-76.

[24] Bagchi, S.; Thorpe, D. G.; Thorpe, I. F.; Voth, G. A.; Fayer, M. D., *J. Phys. Chem. B* **2010,** *114*, 17187-93.

[25] Finkelstein, I. J.; Ishikawa, H.; Kim, S.; Massari, A. M.; Fayer, M. D., *Proc. Natl. Acad. Sci. U. S. A.* **2007,** *104*, 2637-42.

[26] Hunt, N. T.; Greetham, G. M.; Towrie, M.; Parker, A. W.; Tucker, N. P., *Biochem. J.* **2011,** *433*, 459-68.

[27] Ishikawa, H.; Finkelstein, I. J.; Kim, S.; Kwak, K.; Chung, J. K.; Wakasugi, K.; Massari, A. M.; Fayer, M. D., *Proc. Natl. Acad. Sci. U. S. A.* **2007,** *104*, 16116-21.

[28] Ishikawa, H.; Kim, S.; Kwak, K.; Wakasugi, K.; Fayer, M. D., *Proc. Natl. Acad. Sci. U. S. A.* **2007,** *104*, 19309-14.

[29] Merchant, K. A.; Noid, W. G.; Akiyama, R.; Finkelstein, I. J.; Goun, A.; McClain, B. L.; Loring, R. F.; Fayer, M. D., *J. Am. Chem. Soc.* **2003,** *125*, 13804-18.

[30] Thielges, M. C.; Chung, J. K.; Fayer, M. D., *J. Am. Chem. Soc.* **2011,** *133*, 3995-4004.

[31] Andersen, J. F.; Weichsel, A.; Balfour, C. A.; Champagne, D. E.; Montfort, W. R., *Structure* **1998,** *6*, 1315-1327.

[32] Lynch, M. S.; Slenkamp, K. M.; Cheng, M.; Khalil, M., *J. Phys. Chem. A* **2012,** *116*, 7023-32.

[33] Brookes, J. F.; Slenkamp, K. M.; Lynch, M. S.; Khalil, M., *J. Phys. Chem. A* **2013,** *117*, 6234-43.

[34] Ding, X. D.; Weichsel, A.; Andersen, J. F.; Shokhireva, T. K.; Balfour, C.; Pierik, A. J.; Averill, B. A.; Montfort, W. R.; Walker, F. A., *J. Am. Chem. Soc.* **1999,** *121*, 128-138.

[35] Kwak, K.; Park, S.; Finkelstein, I. J.; Fayer, M. D., *J. Chem. Phys.* **2007,** *127*, 124503.

[36] Cheng, M.; Brookes, J. F.; Montfort, W. R.; Khalil, M., *J. Phys. Chem. B* **2013**.

[37] Reichardt, C., *Chem. Rev.* **1994,** *94*, 2319-2358.

[38] Kondrashov, D. A.; Montfort, W. R., *J. Phys. Chem. B* **2007,** *111*, 9244-52.

[39] Sharma, V. S.; Traylor, T. G.; Gardiner, R.; Mizukami, H., *Biochemistry* **1987,** *26*, 3837-3843.

[40] Deflores, L. P.; Ganim, Z.; Nicodemus, R. A.; Tokmakoff, A., *J. Am. Chem. Soc.* **2009,** *131*, 3385-91.

[41] Fayer, M. D., *Annu. Rev. Phys. Chem.* **2009,** *60*, 21-38.

[42] Kim, Y. S.; Hochstrasser, R. M., *J. Phys. Chem. B* **2009,** *113*, 8231-51.

[43] Baiz, C. R.; Kubarych, K. J., *Opt. Lett.* **2011,** *36*, 187-9.

[44] Petersen, P. B.; Tokmakoff, A., *Opt. Lett.* **2010,** *35*, 1962-4.

[45] Cheng, M.; Reynolds, A.; Widgren, H.; Khalil, M., *Opt. Lett.* **2012,** *37*, 1787-9.

Chapter 3

Development of a Tunable Ultra-Broadband Mid-IR Pulsed Source

The work presented in this chapter has been published in the following article:
Cheng, M.; Reynolds, A.; Widgren, H. and Khalil, M. "Generation of tunable octave-spanning mid-infrared pulses by filamentation in gas media" *Opt. Lett.* **2012,** *37*, 1787-9.

Introduction

3.1.1 Introduction

Intense femtosecond mid-infrared (mid-IR) pulses are a standard component of the spectroscopic toolbox used to probe and control structural dynamics in chemical, biological, and material systems [1]. Mid-IR pulses are routinely generated with the use of commercially available ultrafast Ti:sapphire laser in conjunction with an optical parametric amplifier (OPA) and difference frequency mixing in various nonlinear IR crystals. Typically, the generation of mid-IR pulses begins with the Ti:sapphire laser and is used to pump the OPA, from which two pulses of wavelengths in the near-IR (1 to 2.5 μm) are generated. These two pulses (known as the signal and idler) are then focused into a $AgGaS_2$ crystal. When these pulses are spatially and temporally overlapped, the difference frequency generation (DFG) process occurs and produces pulses with wavelengths in the mid-IR [2]. Typical characteristics of pulses produced in this manner are sub-70 fs pulses with a spectral bandwidth ($\Delta_{\omega_{FWHM}}$) of $\sim 250\ \mathrm{cm}^{-1}$ and μJ levels of pulse energy [3].

In recent years, spectrally broad mid-IR and far-IR pulses have been generated by an alternative method that involves the filamentation of intense femtosecond 800 nm pulses and its harmonics in gases at ambient pressure [4-10]. As the ultrashort pulses are focused in a gas medium, numerous nonlinear processes (such as Kerr-self focusing and plasma defocusing) occurs and generates a plasma filament [11]. Within this plasma (or "white light") filament is the occurrence of the four-wave difference frequency mixing process (4WM, $\omega_{IR} = 2\omega_{800} - \omega_{400}$) that generates mid-IR pulses that are as short as sub-20 fs and have $\Delta_{\omega_{FWHM}} > 2000\ \mathrm{cm}^{-1}$. Depending on the condition of the filament, the four-wave difference frequency mixing process may yield not only spectral broad mid-IR pulses but also radiation in the ultraviolet, visible and terahertz regimes as well [12].

The following is a summary of the work that has been done to develop and characterize a tunable source of broadband mid-IR (BBIR) pulses for femtosecond nonlinear IR spectroscopy. The aspect of tunability comes from containing the filamentation of 800 nm/400 nm (ω/2ω) light fields within a gas cell and controlling the gas medium (air, Ar, Ne, and N_2) and the pressure surrounding the filament. From this source, one can generate sub-20 fs, octave-spanning BBIR pulses tunable from 2–8 μm with spectral width greater than 2000 cm^{-1} [13]. Furthermore, the additional data gathered from the characterization of the source further supports the four-wave mixing (4WM) model for BBIR generation via filamentation.

Setup

3.2.1 Layout for BBIR Generation

In comparison to the established method of pulsed mid-IR generation (with the OPA/DFG combination), the setup for BBIR generation is much more straightforward in design and involves far fewer number of optical components. Figure 3.1 is a basic schematic of the experimental setup for generating BBIR pulses. Beginning with the 800 nm output (~30 fs, 3 mJ, 1 kHz) of a Spectra Physics XP Pro Ti:sapphire regenerative amplifier directed towards the setup, a portion of the fundamental (800 nm, ω) pulse generates the second harmonic (400 nm, 2ω) light in a 0.1 mm Type I β-BBO crystal (BBO-601H, Eskma Optics) with an orthogonal *p*-polarization. The orthogonal polarization of the ω and 2ω fields permits the use of a birefringent calcite crystal (Newlight Photonics) to control the relative timing between the two pulses. The subsequent dual wave plate (WPD08-HF-SP, Newlight Photonics) then rotates the polarization of the ω pulse to match the polarization of the 2ω pulse and the two collinear pulses are focused into a 1.2 m stainless steel gas cell using a 1 m focal length silver concave mirror.

The gas cell is sealed with a 1 mm thick AR coated fused silica (UVFS, 226-1211+3213, Eskma Optics) window and a 2 mm thick BaF_2 window at the entrance and exit ports, respectively. After the gas cell, a modified Thorlabs LB1 beam block obstructs most of the intense visible light without obstructing the BBIR (which is not spatially overlapped with the ω/2ω fields). The BBIR pulse is then collimated and passes through a 3mm AR coated germanium (GE-W-25-3 with 2-10 μm AR coating, ISP Optics) window, which selectively transmits the BBIR (>2 μm) radiation to prevent any residual visible light from reaching the mid-IR detection setup. In addition, it was also used to overlap the BBIR with a HeNe beam.

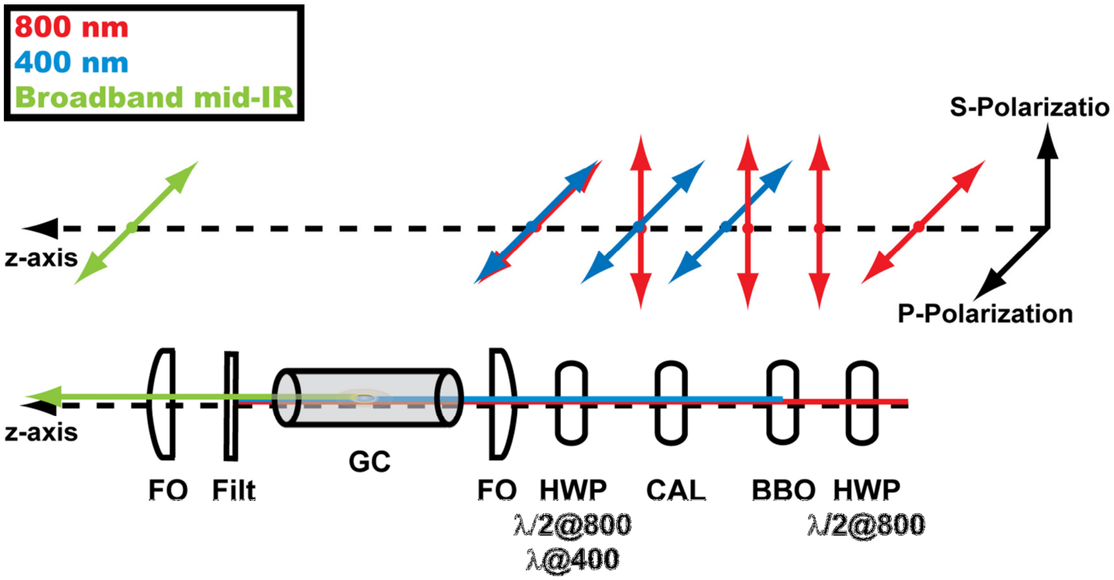

Figure 3.1. The experimental setup for broadband mid-IR generation. The figure has been simplified with the use of a lens instead of reflective concave mirrors to illustrate the focusing of the beams into the cell. The top figure follows the polarization of the various pulses as it travels through the setup. The abbreviations are: HWP, half-wave plate; BBO, beta barium borate crystal; CAL, calcite; FO, focusing optic; GC, gas cell; Filt, mid-IR filter (germanium or silicon window).

Results

3.3.1 BBIR Intensity as a Function of Pressure

Shown in figure 3.2 is the measured BBIR intensity as a function of pressure for the various gases used in this study. With the exception of Ne, all the other gases showed a saturation behavior with respect to pressure. A liquid N_2 cooled HgCdTe detector (MCT-10-0.25, Infrared Associates) was mainly used to measure the BBIR intensity. For higher pulse energies, neutral density (ND) filters placed in front of the MCT detector to insure a linear detector response. At maximum pulse energies, ND filters with a total optical density of 6.7 were employed. The maximum pulse energies were also measured with pyroelectric detectors (LT-020-H, Electro-Optical Systems) which were calibrated against a Coherent J-10MB-LE detector.

The maximum pulse energy measured with the MCT and pyroelectric detectors for generation in air, Ar, Ne and N_2 were 290, 426, 50 and 321 nJ at the respective pressures of 1000, 900, 3800 and 1200 Torr. The stability of the BBIR at the same corresponding pressures were < 2.9% in air, < 4.6% in Ar, < 4.2% in Ne and < 3.3% in N_2. Table 3.1 lists additional parameters of the generated BBIR at the maximum measured pulse energy for each gas.

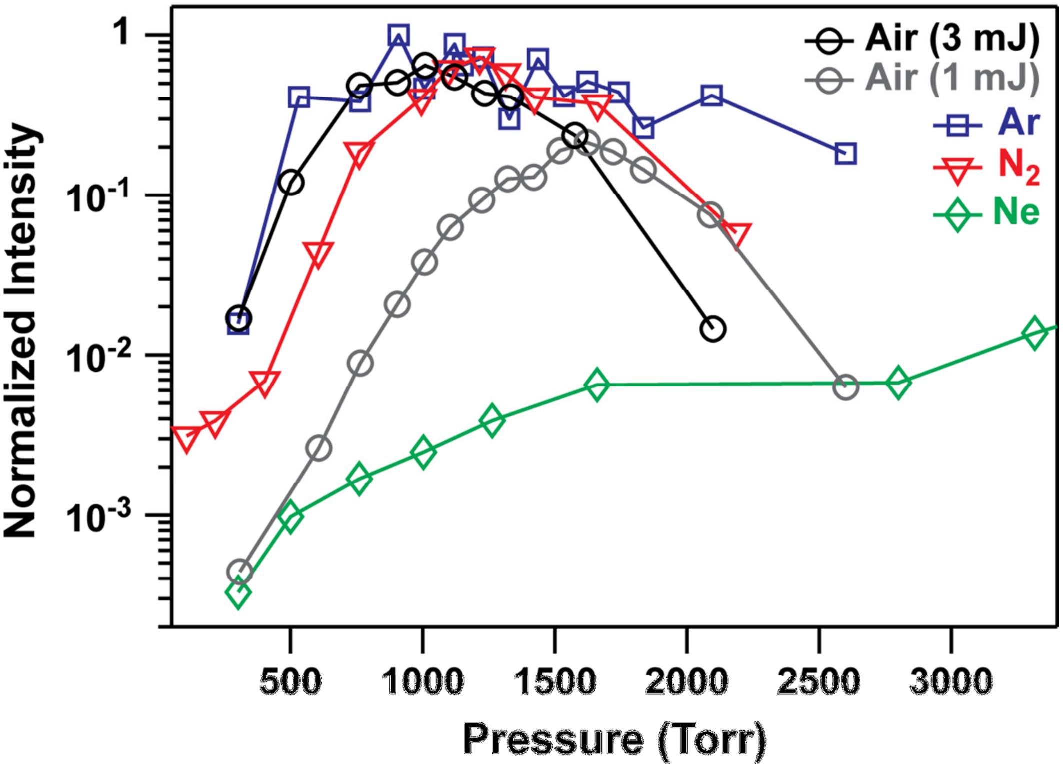

Figure 3.2. The intensity of the BBIR pulse as a function of pressure for various gases ($I_{800\ nm}$ = 3 mJ/pulse).

Gas	**Pressure (Torr)**	λ_{red} **(μm)**	λ_{blue} **(μm)**	**Energy (nJ/pulse)**	**RMS energy fluctuations**
Air	1009	4.0	< 2.6	290	< 2.9 %
Ar	909	3.9	< 2.6	426	< 4.6 %
Ne	3837	6.3	3.2	50	< 4.2 %
N_2	1215	4.8	< 2.6	321	< 3.3 %

Table 3.1. Characteristics of the BBIR source with maximum pulse energies in various gas media with $I_{800\ \mathrm{nm}} = 3$ mJ/pulse. The red (λ_{red}) and blue (λ_{blue}) cut-off wavelengths are measured at 10% spectral intensity. The RMS energy fluctuations were measured for 2.5 hours with 1000 Torr of gas pressure.

3.3.2 Spectral Characterization of the BBIR

The spectral content of the BBIR pulses were characterized by scanning the grating positions of a monochrometer (190 mm monochormeter with a 75 groves/mm grating, Horiba TRIAX 190) and recording the intensity of the individually dispersed spectral component with the MCT detector. To ensure that the measurements were not contaminated with higher diffraction orders from the grating, two additional Ge bandpass filters were employed when the spectral characterization was conducted. The blue (2.5-5.1 μm, BBP-2540-5150c, Spectrogon) and red (4.5-8.5 μm, LP-4500nm, Spectrogon) portions of the BBIR spectrum were scanned separately with the respective filter placed in front of the monochrometer. The final spectra were obtained by piecing the two spectral measurements together while also accounting for the spectral response of the various ND filters used in the measurement.

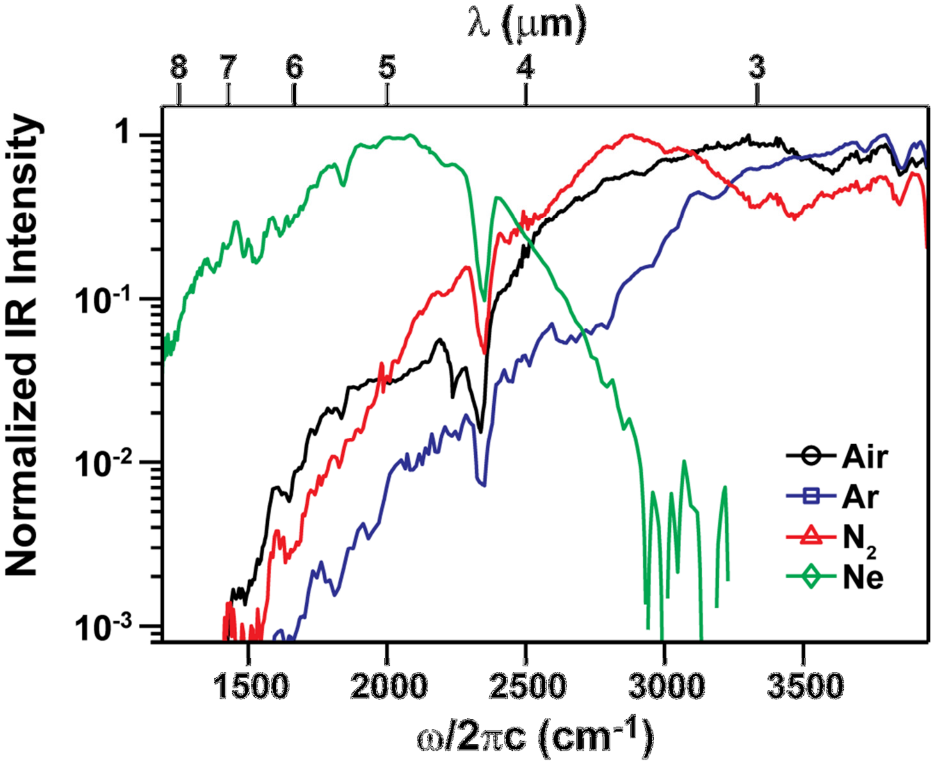

Figure 3.3. The spectral content of the BBIR pulses for various gases at the fixed pressure of 760 Torr ($I_{800\ nm}$ = 3 mJ/pulse).

Figure 3.3 shows the spectral content of BBIR for the various gases at the fixed pressure of 760 Torr. The low-wave pass Ge filter used in our set-up limits our detection of the BBIR pulses to > 2.5 μm and accounts for the abrupt red edge of the spectra shown in the figure. The limited range of the setup may also account for the observed energy turnover point in the previous figure 3.2. The spectrally broadest IR pulse that fits within the experimental window (2.5-8.5 μm) was generated in air at ~300 Torr. BBIR pulses generated under this condition spanned from λ_{blue} = 2.8 to λ_{red} = 7.4 μm. Table 3.2 lists the spectral characteristics and energies of the broadest pulses obtained for each gas at the corresponding pressures.

Gas	**Pressure (Torr)**	**λ_{red} (μm)**	**λ_{blue} (μm)**	**Energy (nJ/pulse)**
Air	304	7.4	2.8	22
Ar	302	6.8	2.8	21
Ne	768	8.0	3.9	41
N_2	325	7.2	3.5	41

Table 3.2. Characteristics of the BBIR source with the broadest spectral content in various gas media with $I_{800\ nm} = 3$ mJ/pulse .

3.3.3 Spectral Tuning as a Function of Pressure

As the pressure of the gas cell increases, the spectral content of the BBIR pulses consistently blueshifts for each gas medium. This trend is illustrated in figure 3.4, which plots the spectral content of the BBIR pulses generated in air at various pressures. Plots of the spectral content as a function of pressure for the other three gases are in the appendix. The insert within figure 3.4 is the spectral tuning curves for the BBIR generated in Air, Ar and N_2. For the case of Ne, the spectral blueshift was not as drastic as the other gases. At the corresponding pressures of 768 and 3740 Torr of Ne, the BBIR pulses have center wavelengths of 5.0 and 4.5 μm respectively. The exact center of the pulses obtained at the higher pressures could not be determined since the spectrum exceeded the limit of our detection (< 2.5 μm).

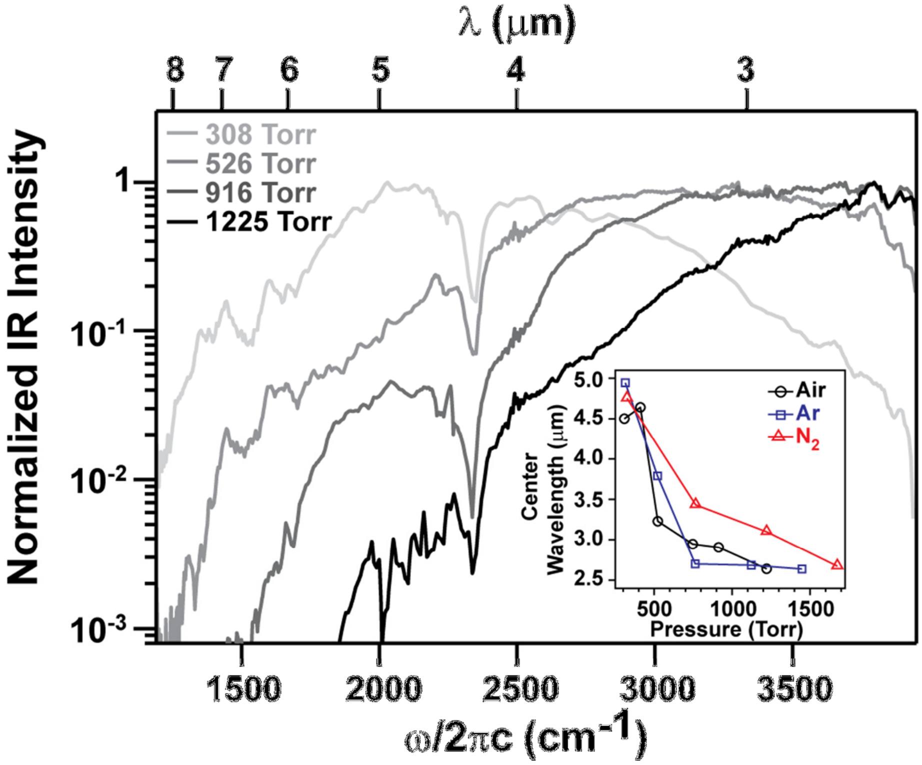

Figure 3.4. BBIR spectra as a function of pressure for air ($I_{800\text{ nm}}$ = 3 mJ/pulse). The inset shows the spectral tuning curves as a function of pressure for various gases.

3.3.4 BBIR Generation as a Function of Fundamental Input Energy

Further investigation was done to examine how the energy and the spectral content of the BBIR pulses varied as a function of the input 800 nm pulse energy. The amount of input energy was controlled using the combination of a half wave-plate and a thin film polarizer that is placed before the BBIR setup. With these optics, the input energy (of the fundamental) can be varied from a minimum of $I_{800\text{ nm}}$ = 0.23 mJ/pulse to a maximum of $I_{800\text{ nm}}$ = 2.6 mJ/pulse. Figure 3.5 displays the spectra of the BBIR pulse as a function of the 800 nm input pulse energy. Similar trends of a corresponding spectral blue shifting (from 3.8 to 3.0 microns) and an increase in BBIR pulse energy (shown in figure 3.9) were observed as $I_{800\text{ nm}}$ increased at the fixed condition of 1000 Torr of air.

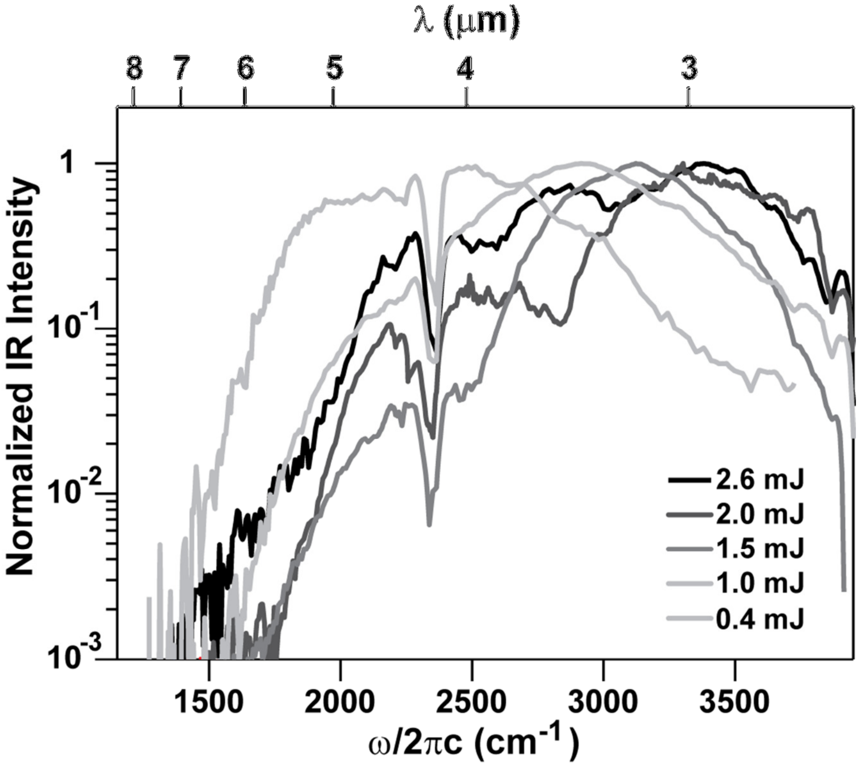

Figure 3.5. The spectral content of the BBIR pulses for various $I_{800\text{ nm}}$ at the fixed pressure of a 1000 Torr of air.

3.3.5 Temporal Characterization with XFROG

Quantitative temporal characterization of the BBIR pulses was done with the cross correlation frequency resolved optical gating (XFROG) technique.[14] Figure 3.6 is a cartoon schematic of the XFROG setup. A 5 μJ portion of the 30 fs, 800 nm pulse from the regenerative amplifier and the BBIR pulse are spatially and temporally overlapped on a 0.1 mm thick lithium niobate crystal (MgO:LiNbO$_3$). The resultant signal generated (due to the sum-frequency generation process) is spectrally dispersed on a spectrometer (Ocean Optics USB 2000+) and collected as a function of the time delay between the 800 nm and the BBIR pulses.

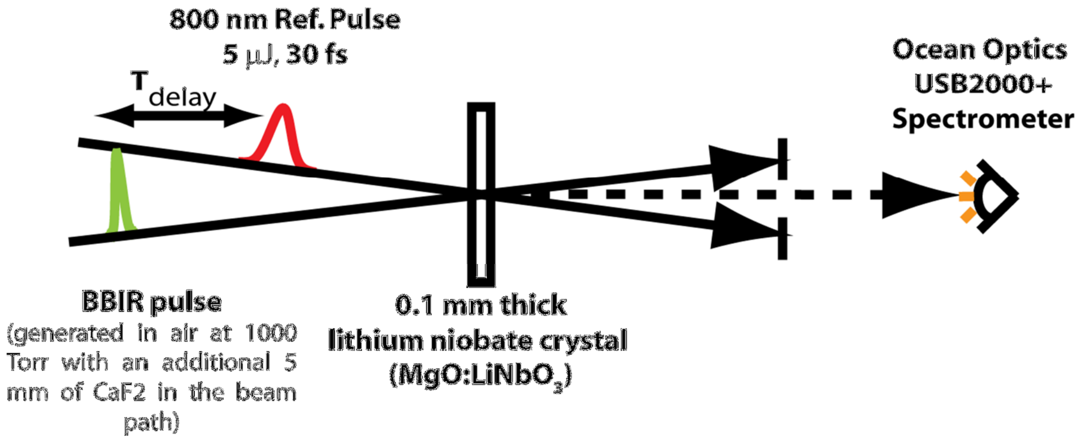

Figure 3.6. A cartoon illustration of the XFROG setup.

Figure 3.7a is the experimental XFROG trace that was collected for BBIR pulses generated under the conditions of 1000 Torr of air with an input energy of $I_{800\ nm}$ = 3 mJ/pulse. Moreover, the LWP Ge filter was replaced with a 250 μm thick Si wafer and an additional 5 mm of CaF_2 was placed in the beam path to balance the group velocity dispersion of the optics. The BBIR electric field was reconstructed using a FROG retrieval algorithm (Femtosoft Technologies) and its FWHM was estimated to be 14 fs as shown in figure 3.7b. This corresponds to a sub 2-cycle pulse centered at 2.4 μm.

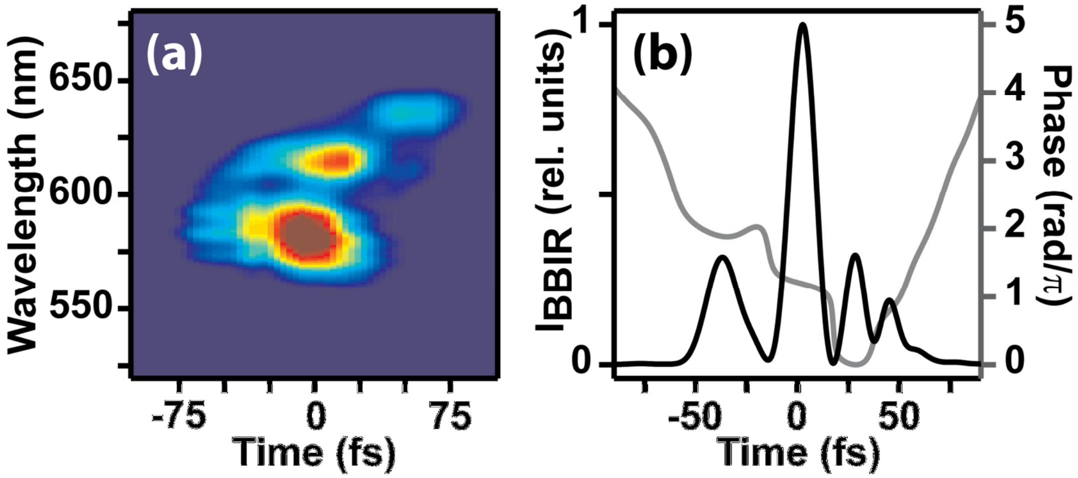

Figure 3.7. (a) The experimental XFROG trace of the BBIR. (b) Reconstructed electric field intensity and phase of the BBIR pulse. The minimum XFROG retrieval error is 0.0175 on a 256 grid.

Discussion and Conclusion

3.4.1 The Use of a Birefrigent Crystal for Temporal Overlap

The use of a birefrigent crystal instead of a mechanical delay line for the ω/2ω temporal overlap simplifies the setup and offers additional phase stability. Figure 3.9(a) shows the dependence of the I_{BBIR} on the relative time delay between the ω/2ω input fields controlled by tuning the angle of the calcite plate. A decrease in BBIR generation efficiency as the time delay exceeded ±50 fs was observed. The ω/2ω temporal walkoff stems from the difference in the group velocity dispersion (GVD) experienced as the two pulses travel through various optical elements and gas medium: β-BBO (+12 fs), λ/2 plate (-12 fs), UVFS window (-160 fs) and the gases (~ -10 fs for Ne and ~ -80 fs for all other gases at 760 Torr).

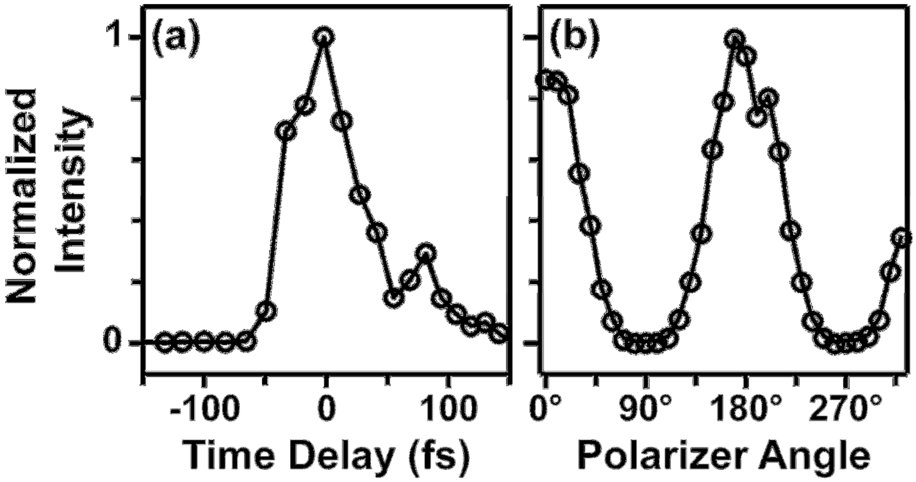

Figure 3.8. (a) The ω/2ω time delay and (b) the analyzer angle. The BBIR pulses were generated in air at 1000 Torr, with $I_{800\ nm}$ = 3 mJ/pulse.

In certain instances, a combination of two identical calcite crystals was used. While a single calcite can theoretically provide the needed temporal delay, the calcite would have to be set at a very steep angle such that it will clip the beam. The use of two calcite crystals not only ensures that neither crystal was ever rotated beyond an angle of 20° from normal but also offers the additional benefit of spatial walk-off compensation. As a result, higher BBIR pulse energy was attained with the use of two crystals (than with one alone) for generation conditions at higher pressures and at higher I_{800}.

The temporal timing was also observed to have an influence on the spectral content of the BBIR pulses as well. As shown in figure 3.8(a), there exists a clear optimal point for the timing as well as broad region in which generation still occurs. Slight changes of the timing in either direction around the maximum favors an enhancement of spectral amplitude on either the blue or red side of the spectrum. However, the overall effect of the timing on the spectra is not as dramatic as the effect of the pressure since it does not shift the center.

3.4.2 Evidence for Four-wave Mixing

The nonlinear process of four-wave mixing (4WM) has been implicated in the generation of not only mid-IR but also of light in the THz regime [5, 8, 10, 12]. The nonlinear polarization giving rise to the BBIR source can be written as:

$$P_j^{(3)} = \chi_{jjjj}^{(3)} E_j(\omega) E_j(\omega) E_j^*(2\omega)$$

where E is the electric field with polarization state, *j*. Since the second harmonic is dependent on the input fundamental ($(E_j(\omega))^2 \propto E_j(2\omega)$), equation above can be also expressed as the following:

$$P_j^{(3)} = \chi_{jjjj}^{(3)} E_j(\omega)^4$$

Furthermore, the electric field amplitude is proportional to the square root of the measured intensity ($E \propto \sqrt{I}$). Hence, the expected relationship between the measured intensity of the BBIR and the input fundamental energy would be:

$$\sqrt{I_{BBIR}} \propto I_{800\,nm}^2$$

Figure 3.9 is a plot of $\mathrm{I_{BBIR}}$ as a function of $\mathrm{I_{800\ nm}}$ and the solid lines in the plot are the fits of the data to the form:

$$\sqrt{I_{BBIR}} \propto I_{800\,nm}^x$$

where x = 1.8 ± 0.4 when $\mathrm{I_{800\,nm}} = 0.2 - 1.0$ mJ/pulse and x = 0.85 ± 0.5 when $\mathrm{I_{800\,nm}} > 1.0$ mJ/pulse. The BBIR power dependence for the input power regime below 1.0 mJ/pulse ($\mathrm{I_{800\,nm}} < 1.0$ mJ/pulse), matches the expected trend and is indicative of the occurrence of the 4WM process.

Finally, the fact that the polarization state of the BBIR is the same as that of the input fields suggests that the BBIR pulse is dependent on the $\chi_{jjjj}^{(3)}$ tensor of the centrosymmetric gas medium. The relative magnitudes of the $\chi_{jjjj}^{(3)}$ tensor for the gases studied here follow the trend of $Ar > N_2 \gg Ne$ at a particular pressure [15]. This explains why the measured BBIR intensity is so much smaller in Ne than the other gases at the same pressure as shown in figure 3.2.

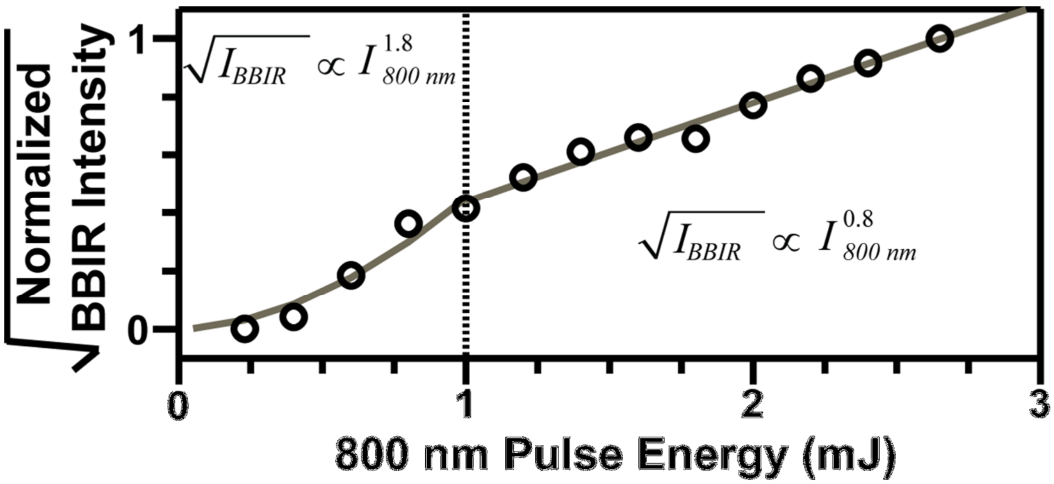

Figure 3.9. BBIR Intensity as a function of $I_{800\ nm}$.

3.4.3 Numerous Nonlinear Processes

Data in figure 3.9 shows that for $I_{800\,nm} > 1.0$ mJ/pulse, x = 0.85 ± 0.05 in $\sqrt{I_{BBIR}} \propto I_{800\,nm}^{x}$ and the numerous causes for this deviation include: the saturation in the 2ω generation, the limited 2-8.5 μm detection window or higher order nonlinear processes occurring in the plasma filament. Given the simultaneous occurrence of numerous processes, it is hard to precisely determine how an individual element (such as the identity of the gas, pressure or input power) affects BBIR generation. For instance, the spectral broadening of both ω/2ω (which is critical to the broad spectral content of the BBIR) was observed with an increase pressure. The cause of the spectral broadening of 2ω could be a pressure enhancement of the cross-phase modulation of the second harmonic or a consequence of the self-phase modulation of the ω.

The peak power density of the ω/2ω pulses for $I_{800\,nm} = 3$ mJ/pulse are on the order of ~10^{14} W/cm^2 before filamentation and it is two orders of magnitude more at the focus. This greatly exceeds the critical power (~10^9 W) required for self-focusing 800 nm femtosecond pulses in air and argon [16]. In addition, the critical power has been shown to decrease with increasing pressure. This may account for the shift of the I_{BBIR} turnover point to a higher pressure for lower $I_{800\text{ nm}}$. As shown in figure 3.2, the turnover point for I_{BBIR} generated in air with $I_{800\text{ nm}} = 1$ mJ/pulse occurs at the higher pressure 1622 Torr, while the turnover for $I_{800\text{ nm}} = 3$ mJ/pulse occurs at a lower pressure of 1009 Torr.

3.4.4 Conclusion

In comparison to this tunable BBIR source, previous reports of mid-IR generation in the 2-8 μm region using intense 800 nm pulses and its harmonics have mostly focused on filamentation in air at ambient pressure with a more conventional delay line between the ω/2ω pulses [4], using a ω/2ω/3ω scheme [6] and demonstration of single shot detection of the BBIR across a 600 cm^{-1} window [3]. In particular, the use of the ω/2ω/3ω scheme and shorter focusing optics (focal length = 5 cm) has resulted in pulses spanning 2-25 μm with only an input of $I_{800\text{ nm}} = 0.4$ mJ/pulse. However, the energy of those BBIR pulses generated are on the order of tens of nanojoules and have an elliptical polarization. Another study has shown the use of pulse-shaping of the input pulses prior to filamentation can change the spectral characteristics of the resultant BBIR [16]. By splitting the fundamental into two colors, one used for SHG and the other mixing for 4WM, one can obtain mid-IR pulses with spectral bandwidth spanning 1-13 μm.

In conclusion, the work done over the last several years has resulted in a sub-20 fs, octave-spanning, spectrally tunable, mid-IR source with stable intensity output based on dual color filamentation in various pressure-controlled gas media. It has been shown that 4WM is the mechanism for generating the linearly polarized BBIR light which has > 0.4 μJ/pulse at 1 kHz. The extensive, spectral and temporal characterization of this source deems it highly suitable for performing spectroscopy and will be employed in transient femtosecond IR and 2D IR spectroscopy on complex molecular systems.

References

[1] Fayer, M. D., *Ultrafast Infrared And Raman Spectroscopy*. CRC Press: 2001; Vol. 26.

[2] Seifert, F.; Petrov, V.; Woerner, M., *Opt. Lett.* **1994,** *19*, 2009.

[3] Kaindl, R. A.; Wurm, M.; Reimann, K.; Hamm, P.; Weiner, A. M.; Woerner, M., *J. Opt. Soc. Am. B* **2000,** *17*, 2086.

[4] Baiz, C. R.; Kubarych, K. J., *Opt. Lett.* **2011,** *36*, 187-9.

[5] Fuji, T.; Suzuki, T., *Opt. Lett.* **2007,** *32*, 3330-3332.

[6] Kim, K. Y.; Taylor, A. J.; Glownia, J. H.; Rodriguez, G., *Nat. Photonics* **2008,** *2*, 605-609.

[7] Petersen, P. B.; Tokmakoff, A., *Opt. Lett.* **2010,** *35*, 1962-4.

[8] Roskos, H. G.; Thomson, M. D.; Kreß, M.; Löffler, T., *Laser Photonics Rev.* **2007,** *1*, 349-368.

[9] Théberge, F.; Châteauneuf, M.; Roy, G.; Mathieu, P.; Dubois, J., *Phys. Rev. A* **2010,** *81*.

[10] Xie, X.; Dai, J.; Zhang, X. C., *Phys. Rev. Lett.* **2006,** *96*.

[11] Chin, S. L.; Chen, Y.; Kosareva, O.; Kandidov, V. P.; Théberge, F., *Laser Phys.* **2008,** *18*, 962-964.

[12] Cook, D. J.; Hochstrasser, R. M., *Opt. Lett.* **2000,** *25*, 1210-2.

[13] Cheng, M.; Reynolds, A.; Widgren, H.; Khalil, M., *Opt. Lett.* **2012,** *37*, 1787-9.

[14] Linden, S.; Giessen, H.; Kuhl, J., *Phys. Status Solidi B* **1998,** *206*.

[15] Shelton, D., *Phys. Rev. A* **1990,** *42*, 2578-2592.

[16] Chin, S.; Wang, T.; Marceau, C.; Wu, J.; Liu, J.; Kosareva, O.; Panov, N.; Chen, Y.; Daigle, J.; Yuan, S.; Azarm, A.; Liu, W.; Seideman, T.; Zeng, H.; Richardson, M.; Li, R.; Xu, Z., *Laser Phys.* **2012,** *22*, 1-53.

Appendix

3.A.1 Spectra of BBIR Pulses Generated in Ar, N_2 and Ne Gas as a Function of Pressure

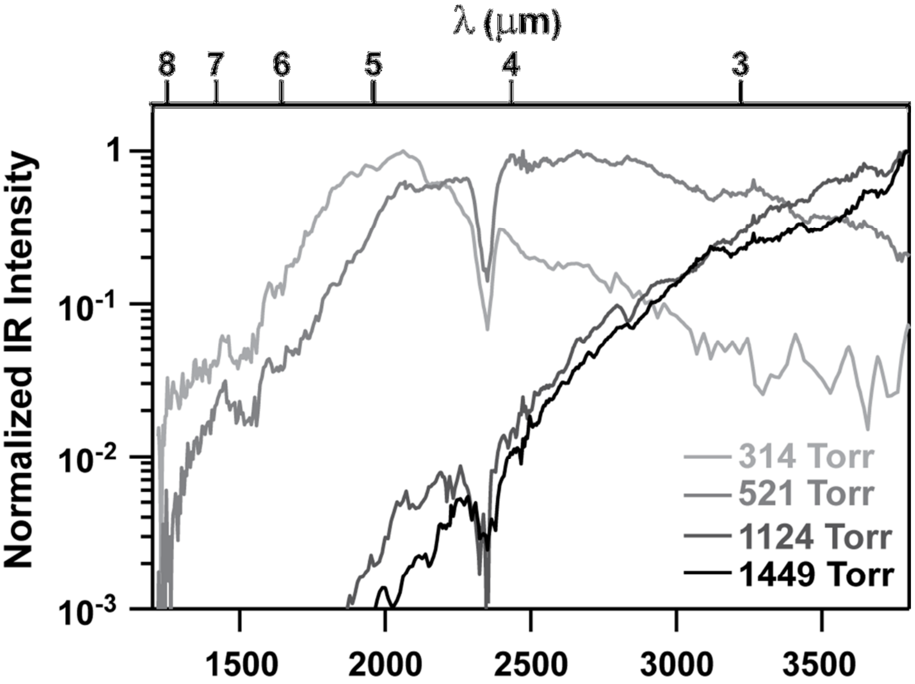

Figure 3.A.1. Spectral content of the BBIR as a function of pressure in argon.

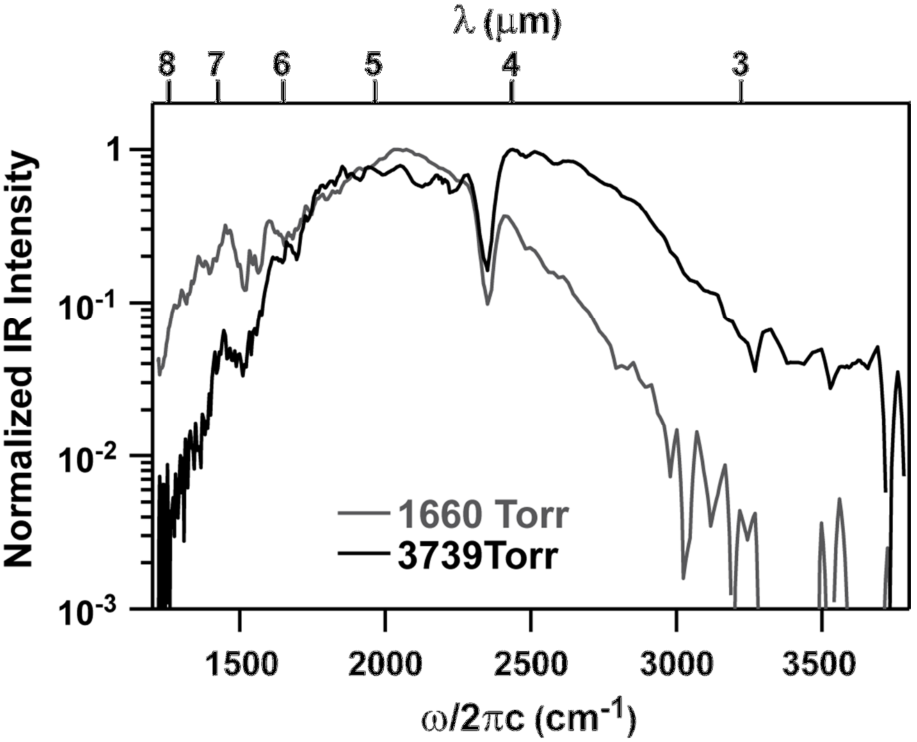

Figure 3.A.2. Spectral content of the BBIR as a function of pressure in neon.

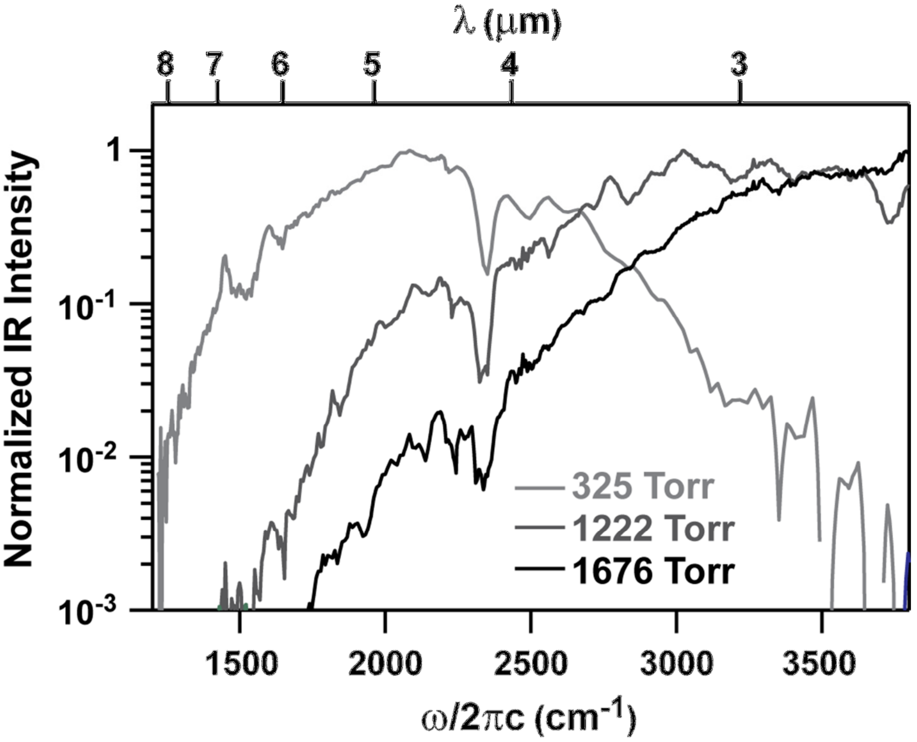

Figure 3.A.3. Spectral content of BBIR as a function of pressure in nitrogen.

Chapter 4

Integration of Broadband IR Source in a Multidimensional Spectroscopy Setup

Introduction

4.1.1 Motivation

Although the amount of information that can be obtained with linear FTIR spectroscopy is limited, one of the few advantages it still has over 2D IR spectroscopy is the ability to probe multiple vibrations simultaneously. The typical spectral window of a conventional FTIR spectrometer (such as the Jasco FT/IR-4100) can span from $400 - 4000 \text{ cm}^{-1}$. In comparison, mid-IR femtosecond pulses generated from source comprised of an Optical Parametric Amplifier and Difference Frequency Generation (OPA/DFG) have a spectral bandwidth ($\Delta_{\omega_{\text{FWHM}}}$) of $\sim 250 \text{ cm}^{-1}$, a temporal bandwidth of sub-70 fs and output pulse energy on the μJ levels [1]. Great strides were made to overcome this source limitation by developing a spectrally broad and tunable mid-IR pulse source. Pulses from this source have spectral bandwidths $\Delta_{\omega_{\text{FWHM}}} > 2000 \text{ cm}^{-1}$ and temporal bandwidths that are sub-15 fs [2]. Although the spectral window is still not as wide as a FTIR spectrometer, the pulses can be tuned to cover the spectral range of > 1250 cm^{-1} to < 5000 cm^{-1}.

One of the challenges in implementing this tunable broadband mid-IR (BBIR) source for multidimensional spectroscopy is the low output pulse energy, which outputs no more than 0.5 μJ/pulse. To overcome this limitation, the new multidimensional spectrometer utilizes two different mid-IR sources arranged in the pump-probe layout: with pump pulses from an OPA/DFG source and probe pulses from the BBIR source. In the pump-probe arrangement, the signal is intrinsically heterodyned by the probe. Given that the pulse energy (of the probe) is typically attenuated to prevent the detector from saturating, the low pulse energy of the BBIR is no longer a significant issue.

The use of the BBIR source extends the ability of 2D IR spectroscopy to coherently probe coupling between numerous vibrational modes. The preliminary work presented here and other recent reports has successfully demonstrated the implementation of BBIR pulses in this manner [3, 4].

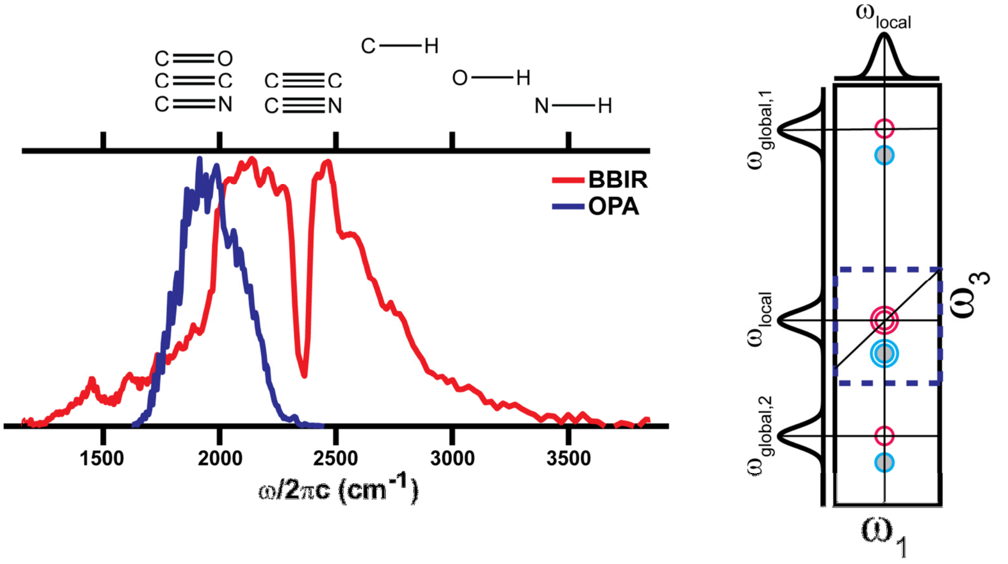

Figure 4.1. (a) Comparison of the spectral bandwidth of a mid-IR pulse from an OPA/DFG and a broadband generation in 406 Torr of air. (b) A cartoon illustration of a 2D IR spectrum using narrowband pump (from an OPA/DFG source) and broadband probe (from a BBIR source) pulses. The dotted box highlights the limited vibrational coherences with a narrowband probe.

Implementation of BBIR Probe in the Experimental Setup

4.2.1. Multidimensional Spectroscopy in the Pump-Probe Geometry

Shown in figure 4.2(a) is the layout of the spectrometer setup that utilizes two different mid-IR pulse sources. Narrowband pulses from the OPA/DFG source are designated as the “pump” pulse while BBIR pulses are designated as the “probe.” The spatial arrangement of the pulses in the pump-probe (or crossed-beam) geometry is shown in figure 4.2(b).

In this setup, a single narrowband IR pulse enters the interferometer and is split into two replica pump pulses. A relative time delay (τ_1) between these two pump pulses is created with a mechanical stage (Newport XMS50) that moves one of the pulses while the other remains static. The two pulses are then recombined on a beamsplitter and travel collinearly along the remainder of the path to the sample. Another mechanical stage (Newport ILS200LM) is used to create the time delay (τ_2) between the pump pulses and the stationary BBIR probe pulse.

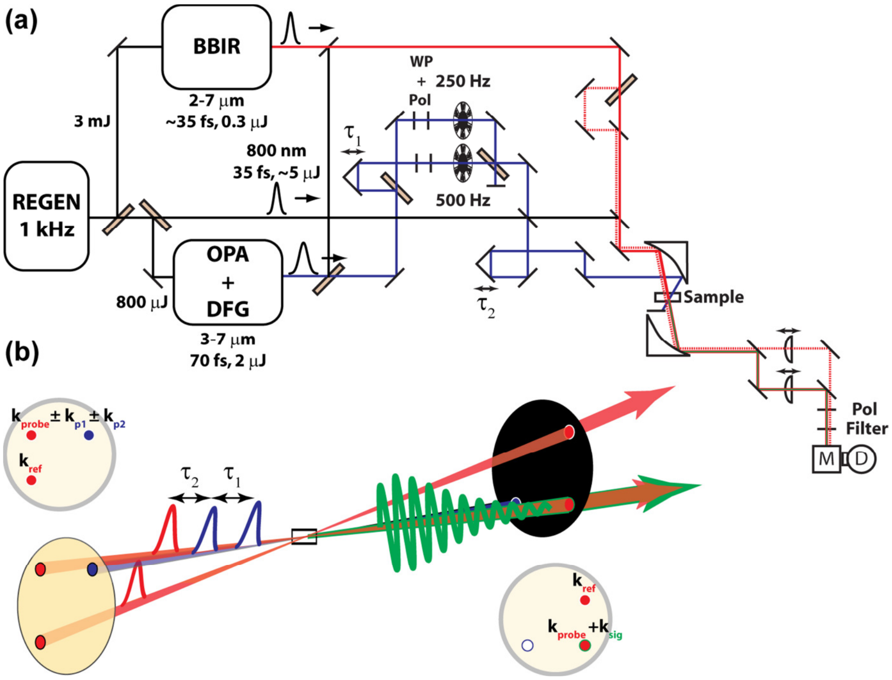

Figure. 4.2. (a) The multidimensional spectrometer in pump-probe layout. Pump pulses (blue) are generated from an OPA/DFG source, while the probe pulses (red) is generated from the BBIR source. The red dotted line represents the reference probe pulse generated from a reflection off a CaF_2 window and is displaced vertically from the probe. The reference probe and signal/probe are then spectrally dispersed by a monochrometer and each is detected individually on the 2 x 64 MCT array detector. (b) The spatial arrangement of the pulses in the pump-probe geometry.

When the three beams are focused at the sample, a third-order nonlinear signal is emitted and is intrinsically self-heterodyned by the probe. The signal and probe travel collinearly towards the detection setup and are focused into a monochrometer (Triax 190, Horiba Jobin Yvon, 75 lines/mm grating). The monochrometer spectrally disperses the signal/probe onto a single strip of a 2 × 64 mercury cadmium telluride (MCT) array detector (IR0144, Infrared Systems Development). To increase the signal-to-noise, a mechanical chopper is placed in each of the pump arms to collect different signals, which are then processed to isolate the signal of interest. In addition, the signal is divided by a reference pulse to normalize intensity fluctuations. This reference probe beam is generated by a reflection off an uncoated CaF_2 window and displaced vertically from the signal/probe.

4.2.2 Comparison between Pump-Probe and Boxcar Geometry

Previous experiments that were conducted by the group (which include the Nitrophorin-4 study) employed a spectrometer setup arranged in the boxcar layout as illustrated in figure 4.3(a) [5-10]. In this setup, a single pulse from the output of the DFG/OPA source enters a spectrometer and creates three identical IR pulses that are spatially situated in three corners of a box (as illustrated in figure 4.3(b)). The emitted background-free homodyne signal appears at the forth corner.

Two additional pulses are also generated within this spectrometer. An additional pulse known as the Tracer outlines the path of the signal and is used for alignment purposes only. Another pulse known as the Local Oscillator (LO) is created and overlapped with the signal field on a beamsplitter. Heterodyne detection in this manner permits independent control of the LO intensity without attenuating the signal itself. Furthermore, the overlapping of the signal and the local oscillator with a beamsplitter results in two identical heterodyned signals (transmitted and reflected) that are π out-of-phase with respect to each other. This permits the use of the “balanced detection” method (as outlined in Ref [8]) that results in the subtraction of the phase-independent intensity fluctuations and further enhancing the overall signal.

In order to obtain fully absorptive spectra with this multidimensional spectrometer, one needs to repeat the experiment twice. The rephrasing (R) and non-rephasing (NR) experiments are conducted by reversing the time-ordering of the first two pulses. Over the length of the experiment, the timing between the LO and signal (τ_3) and the timing between the two first pulses (τ_1) will drift, resulting in phase ambiguities. To correct this, the projection of the 2D IR spectrum along the ω_3 dimension is compared with a two-beam dispersed pump-probe spectrum collected at the same τ_2 time points. However, this correction is not completely infallible and if it is not done properly, phase ambiguities result in false distortions of lineshapes and spectral artifacts.

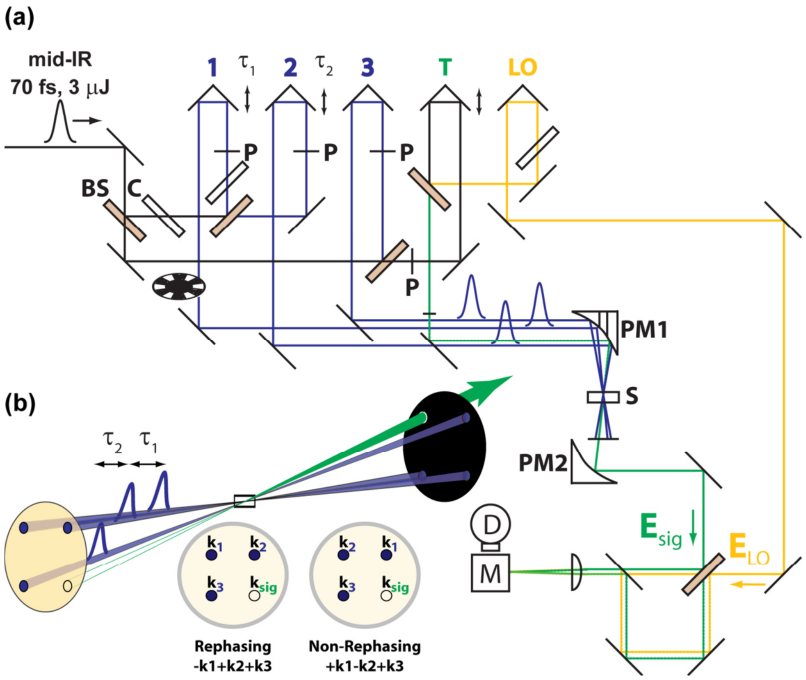

Figure 4.3. (a) The multidimensional spectrometer in the boxcar layout. (b) The spatial arrangement of the pulses in the boxcar geometry.

The strength of the pump-probe layout is its ability to collect purely absorptive spectra. In this arrangement, the coherence pathways for R and NR signals are emitted in the same direction and are indistinguishable with the time ordering of the pulses. Moreover, since the nonlinear signal is intrinsically heterodyned with the probe, phase ambiguity along τ_3 is eliminated (although phase ambiguity along τ_1 still occurs).

4.2.3 Flexibility of the Multidimensional Spectrometer Setup

Great care and much time was spent in the design of the spectrometer setup on Autodesk Inventor. Factors such as the minimization of path length, reduction of footprint and ease of access to the sample and detector were all taken into consideration while ensuring the path lengths of each arm were matched. The setup was also designed with the ability to conduct experiments with the OPA/DFG source only. A narrowband pump pulse can be created by flipping the beamsplitter situated before the interferometer setup. The ability to perform XFROG diagnostic measurements on either the pump or the probe pulse was incorporated into the setup as well (as illustrated in figure 4.4).

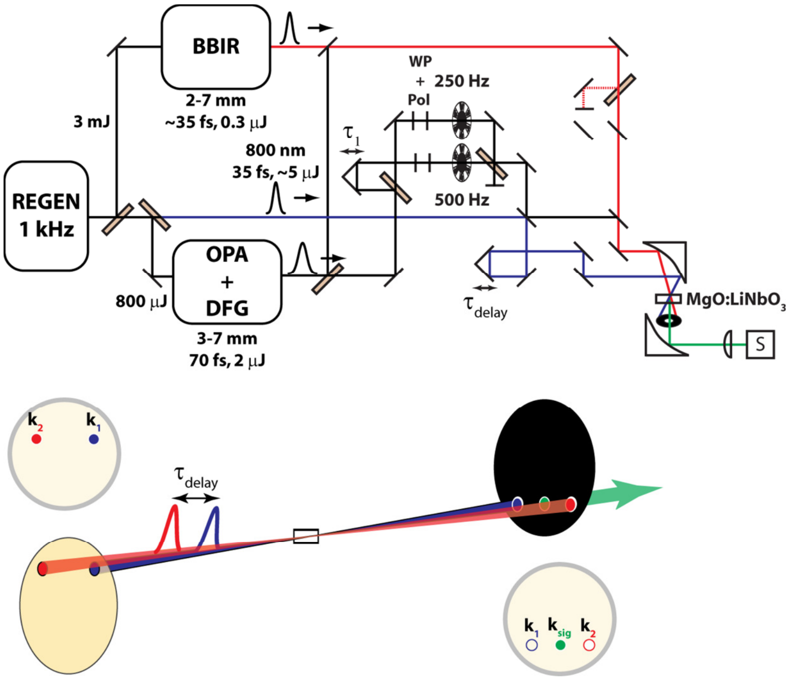

Figure. 4.4. Schematic layout of the XFROG setup for BBIR pulses. Residual fundamental (800 nm) pulses are directed towards the setup and eventually travel along the path of the pump pulse. When the two beams are focused into a 0.1 mm thick lithium niobate crystal ($MgO:LiNbO_3$), a signal is generated by Sum Frequency Generation (SFG). This signal is then collected with a spectrometer for a range of time delays to construct a full XFROG trace.

4.2.4 Optimal Pulse Compression

The shortest temporal duration of any given light pulse is determined by the (Fourier) transform limit of its frequency spectrum. For example, BBIR pulses generated in 550 Torr of air with spectral content centered at ~3.6 μm and a spectral bandwidth ~1500 μm (as shown in figure 4.5) have minimum time duration of ~13 fs. However, pulse duration often deviate from this minimum due to the variations in the spectral phase, stemming from group velocity dispersion (GVD) experienced by the pulse as it propagates through material.

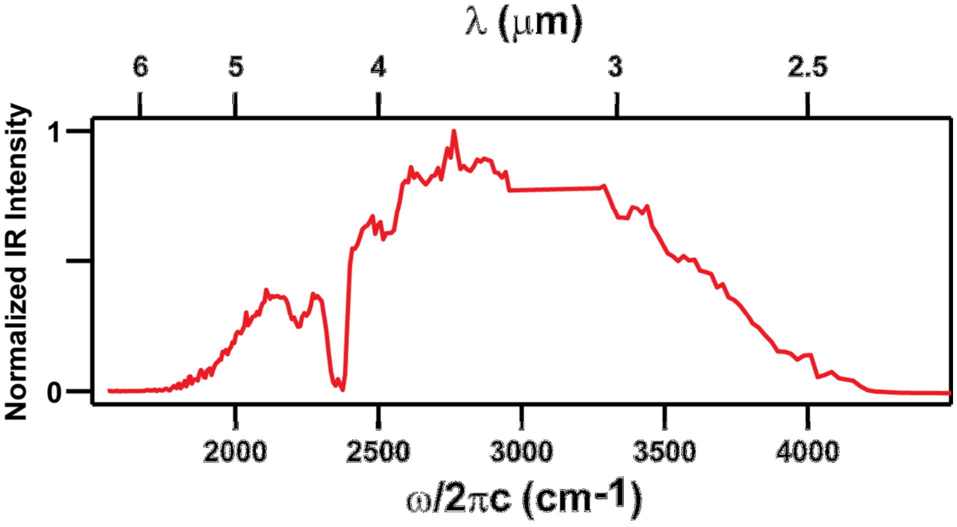

Figure 4.5. The spectral content of BBIR pulses generated under 550 Torr of air.

Ideally, BBIR pulses generated would be temporally compressed by adjusting the grating compressor of the regenerative amplifier. Temporal compression in this manner compresses the BBIR pulses indirectly since adjustments to the grating compressor directly affect the spectral phase of the fundamental (800 nm). Nevertheless, pulses compressed in this manner have the shortest temporal duration of ~25 fs (corresponding to a sub-2 cycle pulse) as shown in figure 4.6(c-d). However, this manner of adjustment has been reserved for the temporal compression of the narrowband IR pulse since the stability and pulse energy of OPA/DFG source is much more sensitive. As a result, BBIR pulses are alternatively compressed with material compensation to negate the GVD experienced, mainly from the 1 mm BaF_2 exit window of the cell and the 400 μm Si visible filter. With an additional 400 μm Si wafer in the BBIR beam path, the resultant pulse durations are as short as ~50 fs (as shown in figure 4.6(e-f)).

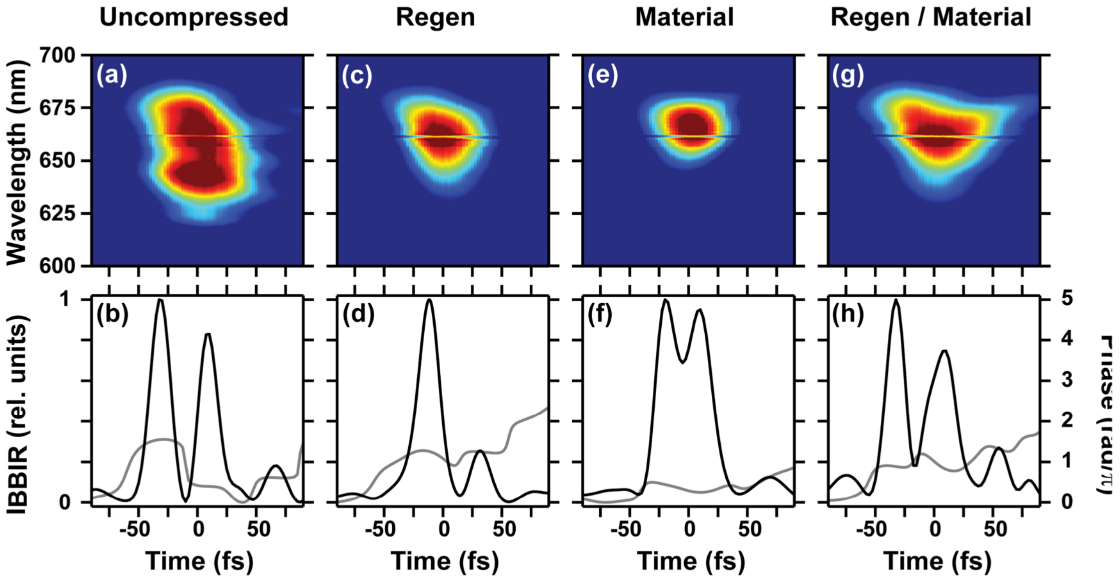

Figure 4.6. A comparison of the different methods used to temporally compress BBIR pulses generated in 550 Torr of air. The temporal characterization was done with the XFROG technique on a 512 grid. Figures (a-b) are the XFROG trace and the reconstructed electric field intensity and phase of the uncompressed pulses (retrieval error = 0.0094). The temporal chirp can be optimized with (c-d) the compressor grating in the regenerative amplifier (r. err. = 0.0090) or with (e-f) material compensation (400 μm of Si; r. err. = 0.005181). Figures (g-h) is the result of optimization when both the compressor grating and material compensation were used (r. err. = 0.0135).

Preliminary IR Pump-BBIR Probe Spectroscopy of the Benzoic Acid Dimer System

4.3.1 Motivation

To test the feasibility of the setup, the deuterated benzoic acid dimer (BA-d_5) was chosen to be the inaugural molecule of study. The use of the BBIR source to study this hydrogen bonded system is an additional direction the lab will take alongside studies of proteins. Hydrogen bonded systems are studied with great interest as they provide valuable insight on hydrogen bonds, which is key to understanding how numerous chemical and biological processes occur [11-23].

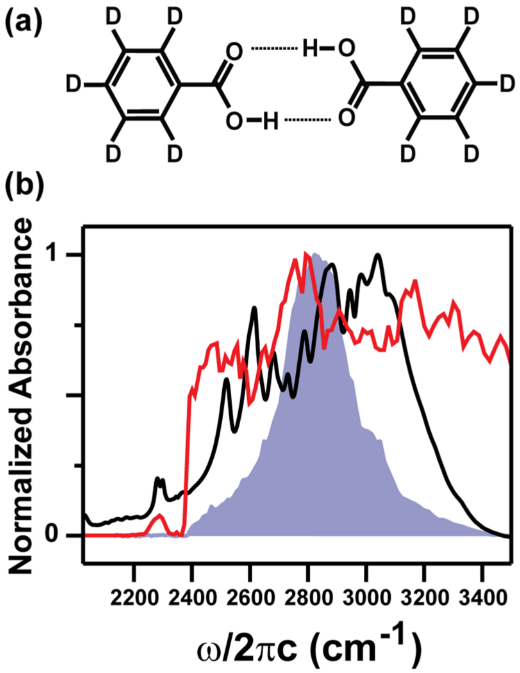

Figure 4.7. (a) The deuterated benzoic acid dimer (BA-d_5). (b) Spectra of the BA-d_5 (black line), mid-IR pump pulses from the OPA/DFG (grey shaded) and BBIR probe pulses (red line).

Previous IR pump-probe experiments and DFT calculations have shown that the O-H stretching vibration, ν_{OH} (~ 2600 cm^{-1} to ~ 3200 cm^{-1}) are coupled to a low-frequency dimer in-plane bending motion (due to H-bond shearing) [22, 23]. This bending motion appears in the pump-probe kinetic time traces as a ~105 cm^{-1} low-frequency oscillation riding on top of the exponential decays. Since narrowband IR pulses were used, these measurements had to be repeated with pulses of different spectral windows to cover the broad ν_{OH} spectral region.

The ability to extract the coupled low-frequency motions across the spectrally broad ν_{OH} will test the feasibility and utility of BBIR source. Polarization IR pump-BBIR probe data were collected under the parallel $\langle 0^{\circ}_{1}, 0^{\circ}_{2}, 0^{\circ}_{3}, 0^{\circ}_{S}\rangle$ and cross $\langle 90^{\circ}_{1}, 90^{\circ}_{2}, 0^{\circ}_{3}, 0^{\circ}_{S}\rangle$ polarization conditions. The collection of polarization selective spectra can be used extract information such as population relaxation and orientational anisotropy [24]. (All references to pump-probe spectroscopy from here on will refer to IR pump-BBIR probe unless explicitly stated).

4.3.2 Setup

Solutions of BA-d_5 were prepared with a solid sample and carbon tetrachloride (CCl_4) solvent purchased from Sigma-Aldrich Co. and used without further purification. Solutions of 0.1 M concentration were sandwiched between two 1 mm CaF_2 windows of a home-built sample cell. The path length of the sample was 300 μm, which resulted in an optical density of 0.4 at ~3037 cm^{-1}.

Pump pulses were generated from a home-built OPA/DFG source. The silver gallium sulfide ($AgGaS_2$) crystal within the DFG portion of the source was tuned to yield narrowband IR pulses with a center wavelength of ~3.6 μm. These pulses have a spectral bandwidth of ~250 cm^{-1} and a temporal bandwidth of ~98 fs (temporally compressed with an additional 1 mm CaF_2 window in the beam path). A half-wave plate (custom optic from ALPHALAS GmbH) and polarizer (WP25H-Z, Thorlabs) were used to control the polarization of the pump pulse. The resultant energy of the pulses with parallel polarization $\langle 0^{\circ}_{\text{pulse}} \rangle$ were 0.299 μJ/pulse while those pulses with cross polarization $\langle 90^{\circ}_{\text{pulse}} \rangle$ were 0.189 μJ/pulse.

Broadband IR (BBIR) probe pulses were generated using the method outlined in Ref [2] with a slight change to the setup: the 100 μm β-BBO crystal was replaced with a thicker 500 μm crystal to generate the second harmonic (400 nm) pulses. BBIR pulses were spectrally tuned to the spectral region of ν_{OH} by surrounding the filament with 835 Torr of air. The cross correlation between the parallel and the cross polarized pump pulses with the BBIR probe pulses indicated an experimental time resolution of ~140 and ~130 fs respectively. The time delay between the pump and probe pulses (τ_{delay}) was accurately controlled with a Newport XMS50 linear stage and was scanned over 134 unequal time points from 0 ps to 6 ps.

The pump-probe signal emitted travels collinearly with the probe and the two were then focused into a monochrometer (Triax 190, Horiba Jobin Yvon, 75 lines/mm grating). Both signals were spectral dispersed onto one of the 2 × 64 stripes of the mercury cadmium telluride (MCT) array detector (IR0144, Infrared Systems Development). A mechanical chopper (operating at 500 Hz) was employed to isolate the pump-probe signal. The chopper was placed in the path of the pump pulse and the detected signals with (the chopper on) and without (the chopper off) the pump were collected and processed. The difference between the two yields the resultant pump-probe signal. At the time of the experiment, the 2nd stripe of the MCT array detector was not functional and as a result, shot-to-shot normalization using the vertically displaced reference field was not performed.

To detect the entire spectral bandwidth of the probe pulse, the pump-probe experiment was repeated at various grating position. A blue (2.5-5.1 μm, BBP-2540-5150c, Spectrogon) and red (4.5-8.5 μm, LP-4500nm, Spectrogon) filter were placed in front of the monochrometer to ensure there is no contamination from higher order diffraction. The final parallel $\langle 0^{\circ}_{1}, 0^{\circ}_{2}, 0^{\circ}_{3}, 0^{\circ}_{S} \rangle$ pump-probe spectrum is comprised from an average of 20 individual scans. For each scan, 1500 pulses were collected at each time delay. Due to the low signal intensity, the final cross $\langle 90^{\circ}_{1}, 90^{\circ}_{2}, 0^{\circ}_{3}, 0^{\circ}_{S} \rangle$ pump-probe spectrum is comprised from an average of 75 individual scans and each scan collected 5000 pulses.

4.3.3 Results

Figure 4.8 is the resultant parallel and cross polarization pump-probe spectra of 0.1 M BA-d_5 in CCl_4. Figure 4.9(a) are slices of the parallel spectrum at various time delays. Not much information can be gathered from these slices without further analysis (which is currently beyond the scope of this work). Figure 4.9(b) are kinetic time traces at selected ν_{OH} frequencies. In these traces, the low-frequency oscillation can be clearly seen.

In order to identify the low-frequency oscillatory component, the kinetic traces were initially fitted to various decaying exponential functions: a single exponential decay with a static component, a double exponential decay or a double exponential decay with a static component. These fits were then subtracted from the actual trace and the resultant residuals were then Fourier transformed. Figure 4.10 are the results of the Fourier transform, which identifies the frequencies of the oscillatory component ($\nu_{\text{Low Freq}}$) for each ν_{OH}.

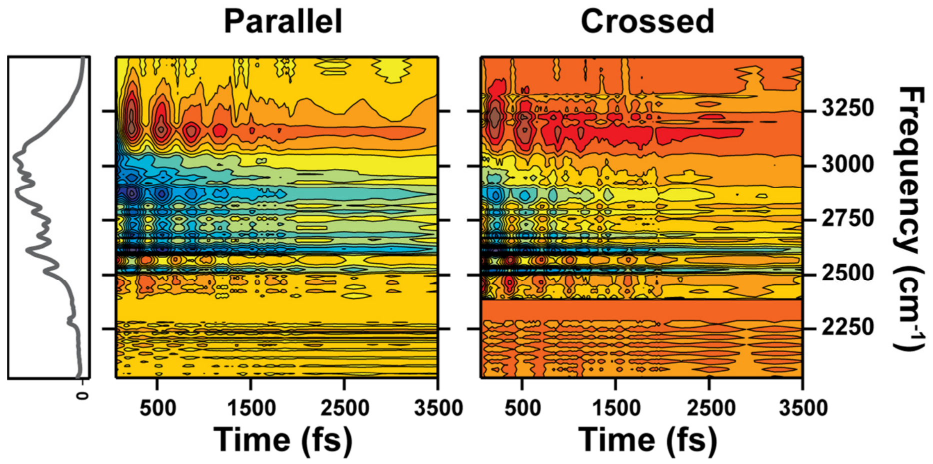

Figure 4.8. The parallel $\langle 0^{\circ}_{1}, 0^{\circ}_{2}, 90^{\circ}_{3}, 90^{\circ}_{S}\rangle$ and cross $\langle 90^{\circ}_{1}, 90^{\circ}_{2}, 0^{\circ}_{3}, 0^{\circ}_{S}\rangle$ polarization IR pump-BBIR probe spectra of 0.1 M BA-d_5 in CCl_4.

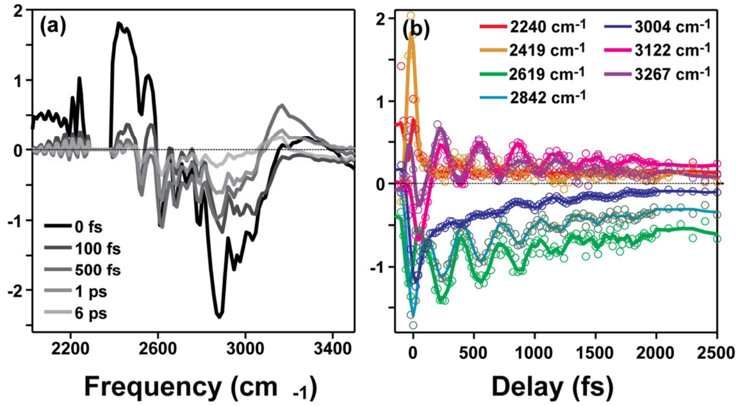

Figure 4.9. (a) Slices of the pump-probe spectra at various time delays. (b) Kinetic traces for a selection of ν_{OH} frequencies.

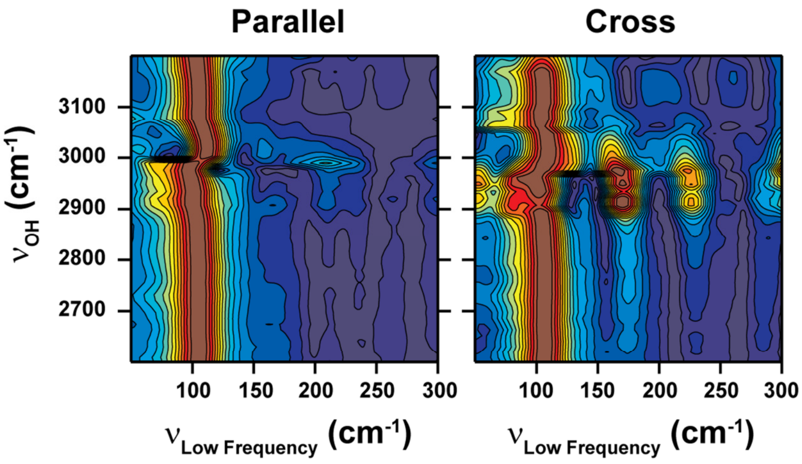

Figure 4.10. A contour plot of Fourier Transform of the residual oscillatory component ($\nu_{Low\ Freq}$) as a function of ν_{OH}.

4.3.4 Discussion and Conclusion

The goal of this experiment was to demonstrate the viability of the BBIR source for applications of multidimensional spectroscopy. The polarization pump-probe experiment produced data that were similar to those from a previous study. While further data analysis of the spectra is beyond the scope of the work, a quick glance of the data reveals additional low-frequency motions that have only been reported from DFT calculations.

The Fourier transform analysis of the oscillatory component indicated that there is additional amplitude for $\nu_{\text{Low Freq}}$ at 110 cm^{-1} in both sets of data and at 170 and 226 cm^{-1} in the cross data only. According to previous DFT calculations, these $\nu_{\text{Low Freq}}$ are due to numerous intermolecular stretching and bending motions (as summarized in table 4.1) [27].

Experimental (cm^{-1})	**DFT (cm^{-1})**	**DFT Assignment**
	85	torsion (−COOH) twisting
105	103	H-bond shearing (in-plane bending)
110	111	(O⋯O) stretching
170	168 (A_u) 175 (B_g)	(Ph-COOH) out-of-plane bending
226	253 (A_g) 276 (B_u)	(CO−O) in-plane bending + (CC) in-plane bending

Table 4.1. The experimentally measured and theoretically calculated $\nu_{\text{Low Freq}}$ modes. The DFT calculated frequencies and assignments are from Ref [27].

Plot of the strongest $\nu_{\text{Low Freq}}$ component for each corresponding ν_{OH} is shown in figure 4.11. What can be clearly observed from this plot is the anticipated shift of the ~105 cm^{-1} $\nu_{\text{Low Freq}}$ to lower frequencies as the ν_{OH} stretching frequency increases. However, it is rather odd that this shift and the appearance of the additional low-frequency modes occur within the ν_{OH} range of 2900 – 3000 cm^{-1}, which is outside the FWHM bandwidth of the pump pulses.

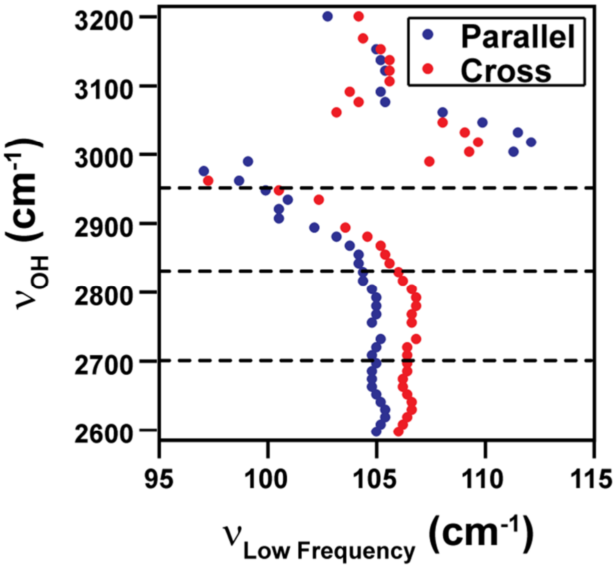

Figure 4.11. A scatter plot of the strongest $\nu_{\text{Low Freq}}$ as a function of ν_{OH}. The dotted lines indicate the center and spectral bandwidth (FWHM) of the mid-IR pump pulses from the OPA/DFG.

2D IR Spectroscopy with the BBIR Source

4.4.1 Introduction

On the heel of a successful demonstration of the BBIR source for IR pump-probe spectroscopy, a demonstration of its use for 2D IR spectroscopy should not be far off. The main difference between an IR pump-probe and a 2D IR experiment is a temporal separation of the two pump pulses (a single pump pulse in an IR pump-probe experiment interacts twice with the sample and is equivalent to two pump pulses with no time delay between them). This is accomplished with the interferometer setup that splits the single pulse into two replica pump pulses and the use of a translation stage (Newport XMS50) to create a relative time delay (τ_1) between the two.

Since previous LabVIEW programs were written specifically for the collection of 2D IR spectra with the boxcar setup, the programs had to be revamped in order to be compatible with the new multidimensional spectrometer. Moreover, to isolate the signal of interest from other third-order nonlinear signals, each of the pump pulses were chopped with a mechanical chopper operating at half (500Hz) and a quarter (250Hz) of the repetition rate of the regenerative amplifier. The use of the two mechanical choppers permits the subtraction of the pump-probe contributions that contaminate the 2D IR signal.

4.4.2 LabVIEW Programing for the "Double-Chopping" Technique

The operation of the detector setup and the mechanical choppers are synced to the 1 kHz repetition rate of the regenerative amplifier (Spectra Physics Spitfire Pro-35F-XP). The 1 kHz TTL signal from the regenerative amplifier is used to trigger the first mechanical chopper operating at 500 Hz. The TTL output of the first chopper is then used to trigger the second mechanical chopper operating at 250 Hz. The phases of the choppers are adjusted so that the pump pulses are aligned to the rise of each corresponding TTL. A total time of 4 ms is needed to collect all the shots necessary to isolate a single shot of the heterodyne signal. At any given moment when the array detector is on, the collection of data can begin with any one of the shots labeled A thru D.

The LabVIEW program identifies the sequence of the shots within each 4 ms window and processes the collected shots accordingly. For example, the yellow box in figure 4.12 indicates the start of the collection of data on shot C. At every 4 ms, the signals collected are as follows: (1) the pump-probe signal from the narrowband pump 1/BBIR probe, (2) the pump-probe signal from the narrowband pump 2/BBIR probe, (3) the two pump-probe signals and the 2D IR signal, and (4) the BBIR probe alone. Figure 4.13 represents the portion of the program that processes the signals collected for this particular sequence.

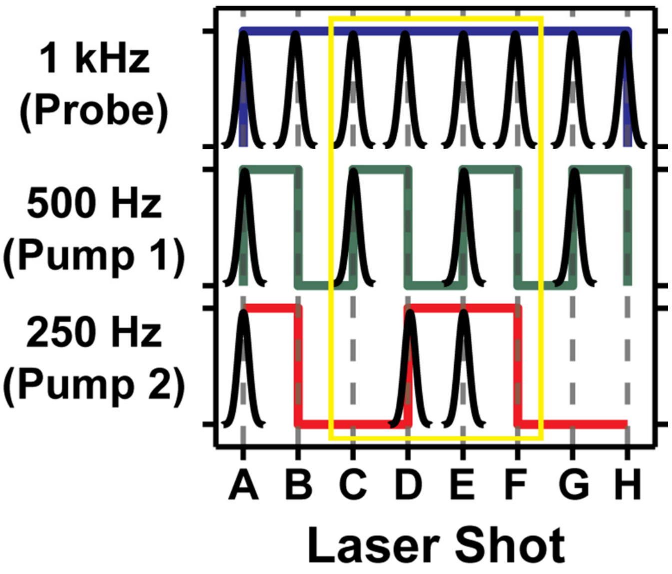

Figure 4.12. The TTL signal of the two mechanical choppers that modulate the pump pulses at a repetition rate of 500 Hz and 250 Hz. The probe pulse is unmodulated and its repetition rate is 1 kHz.

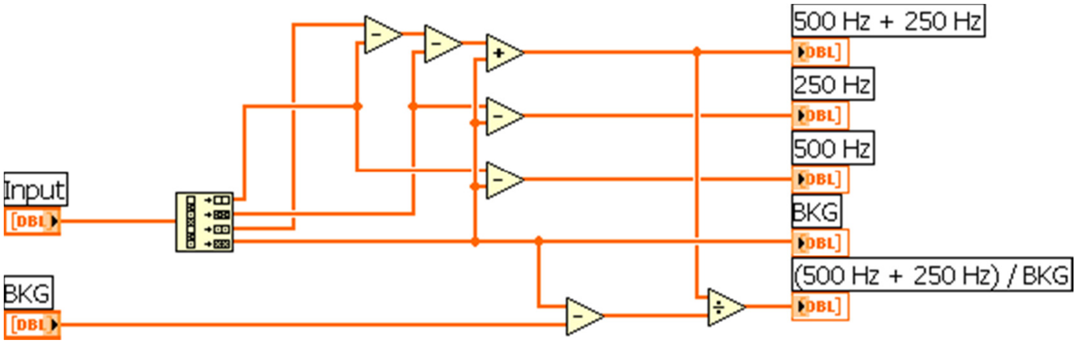

Figure 4.13. The graphical LabVIEW code illustrating the treatment of data collected within the 4 ms window highlighted in figure 4.12. To isolate the 2D IR signal (500 Hz + 250 Hz), the following operation is performed: (500 Hz + 250 Hz) = 3rd shot– (1st shot + 2nd shot − 4th shot). Furthermore, the probe subtracted with an initial dark spectrum and the subsequent division normalizes the intensity fluctuations.

4.4.2 Preliminary Results

The nitrosyl (NO) stretch vibration of sodium nitroprusside (SNP) was used to test the 2D IR setup and programs. A solution of 0.14 mM SNP dissolved in ethanol was prepared and sandwiched between two 1 mm CaF_2 windows of a home-built sample cell (sample path length of 200 μm). Each of the parallel pump pulses were crudely aligned to the BBIR probe at the sample cell. The cross correlation between each of the pumps and the BBIR probe indicated a temporal width of ~127 and ~150 fs.

Shown in figure 4.14 is a comparison of the interferogram collected with this setup at τ_2 = 0 fs and the non-rephasing interferogram collected with the previous boxcar setup that utilized an OPA/DFG source only. Although the signal-to-noise of the new setup was reduced by a factor of 9 for the same concentration of SNP, the nitrosyl peak is still clearly resolved in the resultant 2D IR spectrum at the expected position of ~1905 cm^{-1}.

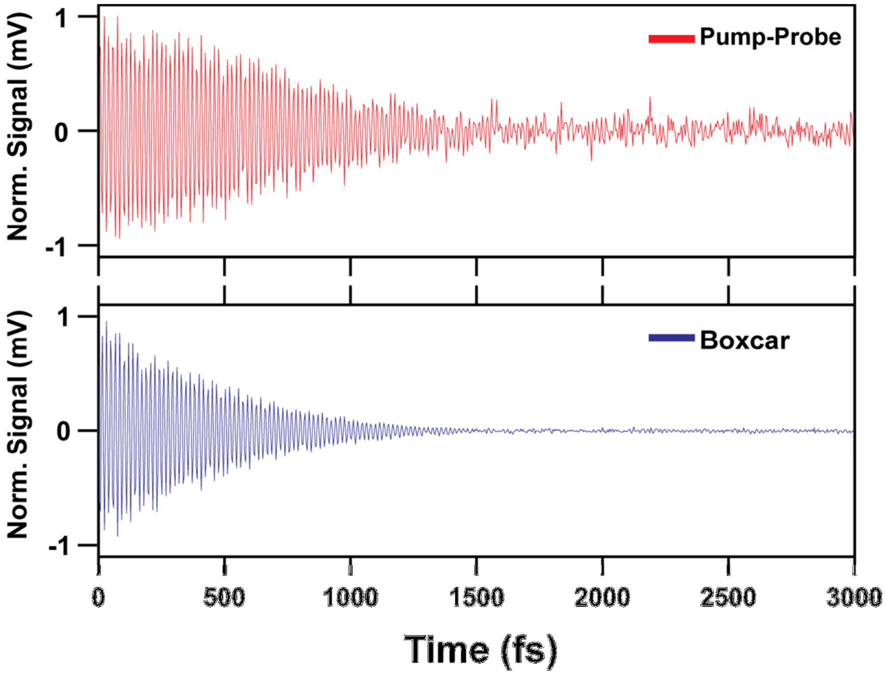

Figure 4.14. (a) Comparison of the signal-to-noise levels of the interferograms obtained from two different 2D IR setups probing 14 mM sodium nitropursside in ethanol. The interferogram (red) is from the pump-probe setup while the (non-rephasing) interferogram (blue) is from the boxcar setup.

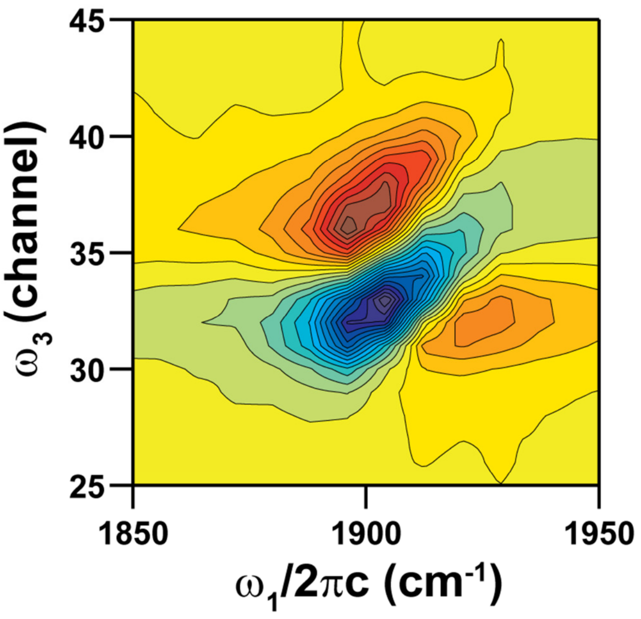

Figure 4.15. The resultant 2D IR spectrum of SNP obtained with the pump-probe setup. The spectrum is comprised of an average of 20 scans. At each τ_1 time point (scanned from $\tau_1 = -40\text{ fs} \rightarrow 3000\text{ fs}$), 2000 shots were collected. The frequency axis ω_3 was not calibrated and is left as the array detector channels.

4.4.3 Future

The initial test of the multidimensional spectroscopy setup using the BBIR source has provided some promising results. There are still many tweaks that can be implemented to further enhance the signal-to-noise, such as independent control of the "local oscillator" intensity and shot-to-shot division with a reference probe [25].

At the moment, the major drawback with the current setup is the need to repeat the experiment at numerous grating positions to cover the broad spectral window of the BBIR pulse. Alternatively, the data can be collected in the full time-domain method by collecting an interferogram for τ_3 and Fourier transform the resultant interferogram to yield the ω_3 axis [26]. It is not clear whether this method is less time intensive than the current method, but detection in this manner forgoes the difficult reconstruction of the spectra across the different grating position and will not be limited by the spectral response of the grating and array detector. Regardless of the direction that will be taken with detection setup, there are numerous biological and hydrogen bonded systems to be studied with this setup in the future to come.

References

[1] Kaindl, R. A.; Wurm, M.; Reimann, K.; Hamm, P.; Weiner, A. M.; Woerner, M., *J. Opt. Soc. Am. B* **2000,** *17*, 2086.

[2] Cheng, M.; Reynolds, A.; Widgren, H.; Khalil, M., *Opt. Lett.* **2012,** *37*, 1787-9.

[3] De Marco, L.; Ramasesha, K.; Tokmakoff, A., *J. Phys. Chem. B* **2013**.

[4] Ramasesha, K.; De Marco, L.; Mandal, A.; Tokmakoff, A., *Nat. Chem.* **2013,** *5*, 935-40.

[5] Brookes, J. F.; Slenkamp, K. M.; Lynch, M. S.; Khalil, M., *J. Phys. Chem. A* **2013,** *117*, 6234-43.

[6] Cheng, M.; Brookes, J. F.; Montfort, W. R.; Khalil, M., *J. Phys. Chem. B* **2013**.

[7] Lynch, M. S.; Cheng, M.; Van Kuiken, B. E.; Khalil, M., *J. Am. Chem. Soc.* **2011,** *133*, 5255-62.

[8] Lynch, M. S.; Slenkamp, K. M.; Cheng, M.; Khalil, M., *J. Phys. Chem. A* **2012,** *116*, 7023-32.

[9] Lynch, M. S.; Slenkamp, K. M.; Khalil, M., *J. Chem. Phys.* **2012,** *136*, 241101.

[10] Lynch, M. S.; Van Kuiken, B. E.; Daifuku, S. L.; Khalil, M., *J. Phys. Chem. Lett.* **2011,** *2*, 2252-2257.

[11] Detoni, S.; Hadži, D., *Spectrochim. Acta* **1964,** *20*, 949-955.

[12] Marechal, Y., *J. Chem. Phys.* **1968,** *48*, 3697.

[13] Druyan, M. E.; Reis, A. H.; Gebert, E.; Peterson, S. W.; Mason, G. W.; Peppard, D. F., *J. Am. Chem. Soc.* **1976,** *98*, 4801-4805.

[14] Walmsley, J. A., *J. Phys. Chem.* **1984,** *88*, 1226-1231.

[15] Flakus, H. T.; Bryk, A., *J. Mol. Struct.* **1995,** *372*, 229-240.

[16] González, L.; Mó, O.; Yáñez, M.; Elguero, J., *J. Chem. Phys* **1998,** *109*, 2685.

[17] Wójcik, M. J.; Boczar, M.; Stoma, M., *Int. J. Quantum Chem.* **1999,** *73*, 275-282.

[18] Wójcik, M. J.; Boczar, M.; Wieczorek, M.; Tatara, W., *J. Mol. Struct.* **2000,** *555*, 165-173.

[19] Wójcik, M. J.; Tatara, W.; Boczar, M.; Apola, A.; Ikeda, S., *J. Mol. Struct.* **2001,** *596*, 207-214.

[20] Flakus, H. T.; Chełmecki, M., *Spectrochim. Acta (A)* **2002,** *58*, 179-196.

[21] Flakus, H. T., *J. Mol. Struct.* **2003,** *646*, 15-23.

[22] Boczar, M.; Szczeponek, K.; Wójcik, M. J.; Paluszkiewicz, C., *J. Mol. Struct.* **2004,** *700*, 39-48.

[23] Yamaguchi, S.; Banno, M.; Ohta, K.; Tominaga, K.; Hayashi, T., *Chem. Phys. Lett.* **2008,** *462*, 238-242.

[24] Tan, H.-S.; Piletic, I. R.; Fayer, M. D., *J. Opt. Soc. Am. B* **2005,** *22*, 2009.

[25] Xiong, W.; Zanni, M. T., *Opt. Lett.* **2008,** *33*, 1371.

[26] Roberts, S. T.; Loparo, J. J.; Ramasesha, K.; Tokmakoff, A., *Opt. Commun.* **2011,** *284*, 1062-1066.

Appendix

4.A.1. Additional Schematic of the Multidimensional Spectrometer Setup

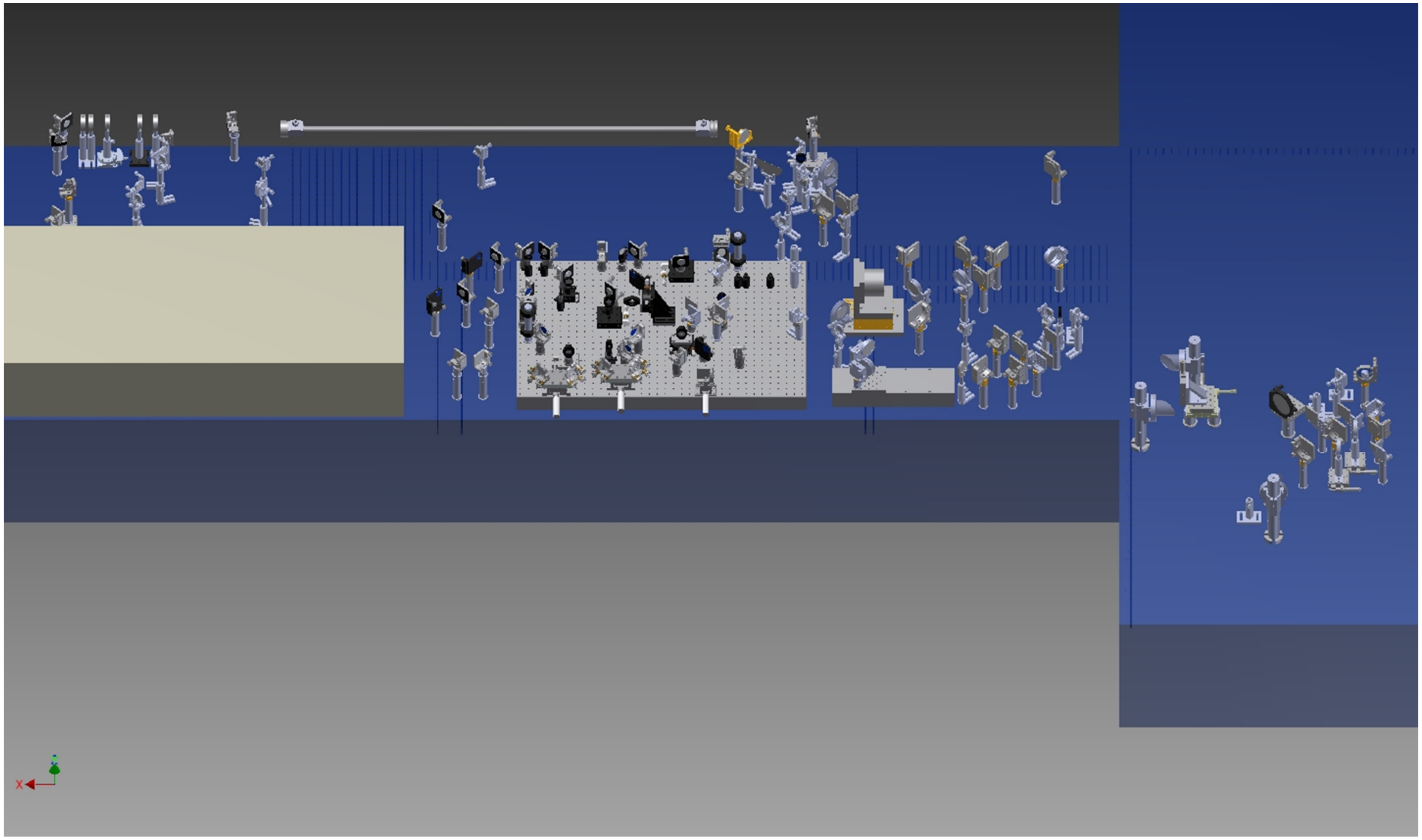

Figure. 4.A.1. Layout of the spectrometer setup from Autodesk Inventor

4.A.2. Additional Diagrams of the LabVIEW Programing

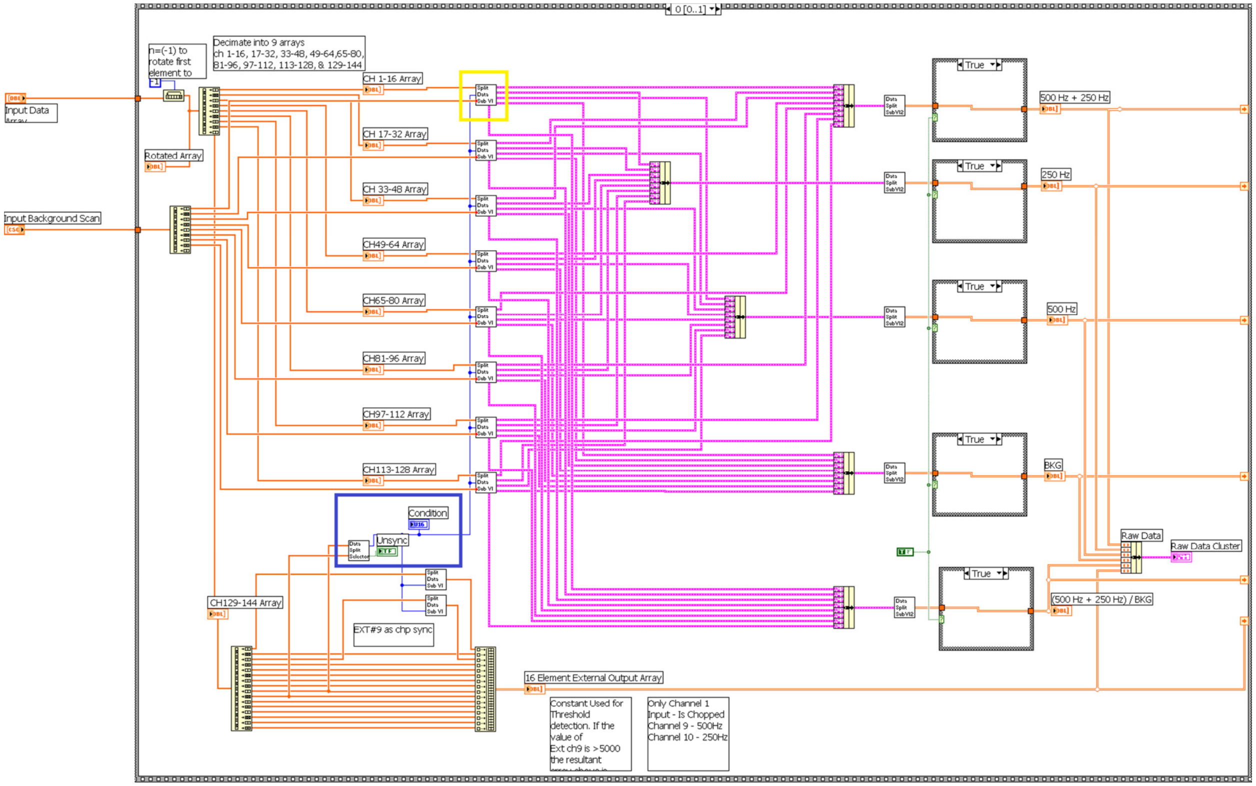

Figure 4.A.2. The main portion of the LabVIEW code written for the 2D IR experiment. The yellow box highlights the sub-VI that processes the collected shots and contains the sub-VI shown in figure 4.13. The blue box highlights the sub-VI used to identify the sequence of shots within each 4 ms time window.

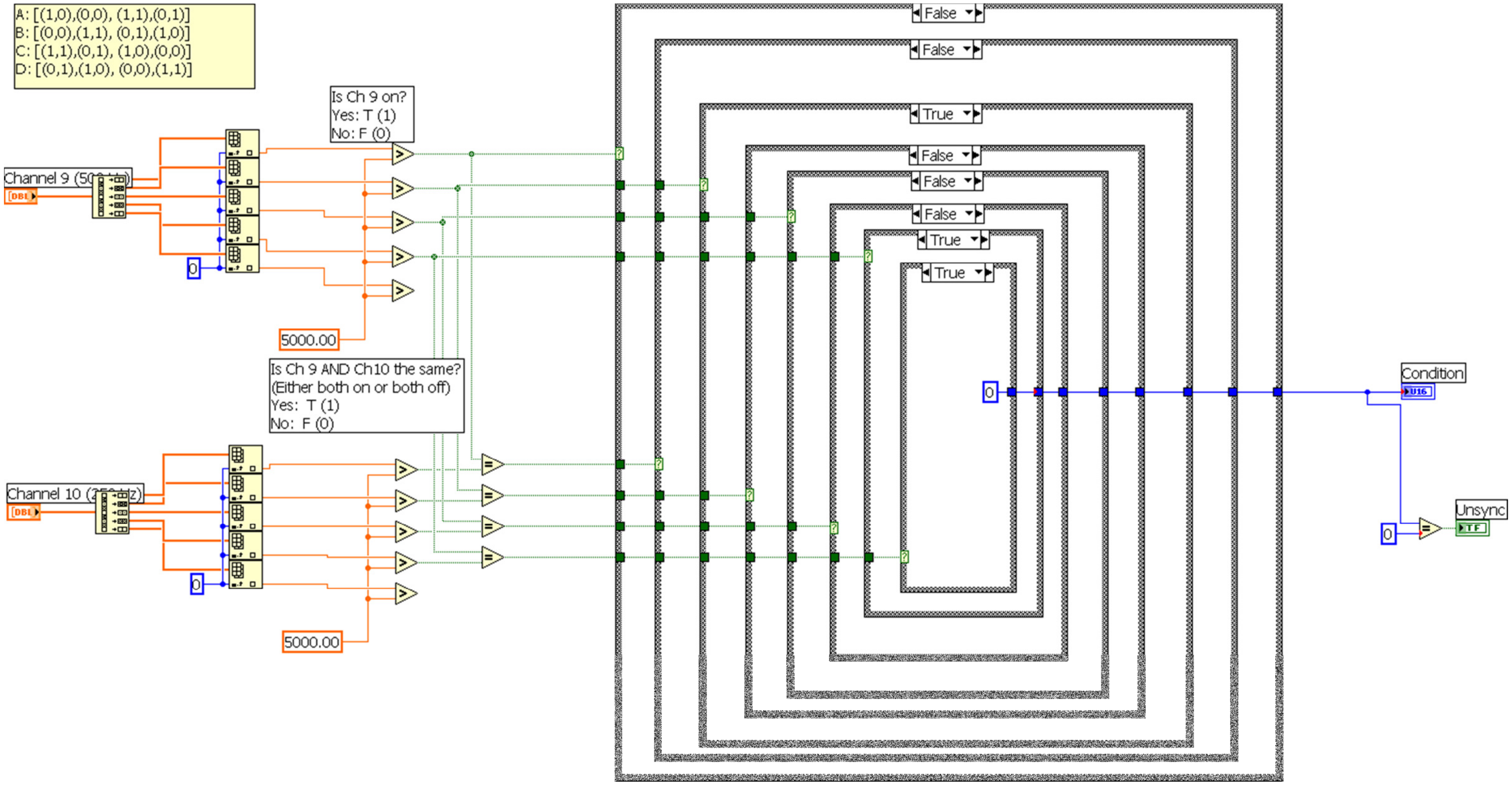

A: [(1,0),(0,0), (1,1),(0,1)]
B: [(0,0),(1,1), (0,1),(1,0)]
C: [(1,1),(0,1), (1,0),(0,0)]
D: [(0,1),(1,0), (0,0),(1,1)]

Is Ch 9 on?
Yes: T (1)
No: F (0)

Is Ch 9 AND Ch10 the same?
(Either both on or both off)
Yes: T (1)
No: F (0)

Figure 4.A.3. The sub-VI that identifies the sequence of the shots within each 4 ms time window by examining the TTL signal from the 500 Hz and 250 Hz mechanical choppers.

Mark Cheng

EDUCATION:

2008-2013 University of Washington, Seattle, WA
Doctor of Philosophy, Physical Chemistry

2000-2004 State University of New York at Stony Brook
Bachelor of Science, Chemistry and Physics
Cum laude

1996-2000 Brooklyn Technical High School, Brooklyn, NY
Regents High School Diploma

TEACHING EXPERIENCE:

9/13 – Teaching Assistant
9/08 – 6/09 Dept. of Chemistry
University of Washington, Seattle, WA

6/13 – 8/13 STEM Study Section Instructor
UW Math Science Upward Bound David Wolczyk
University of Washington, Seattle, WA

8/07 – 7/08 MGI GEAR Up 8th Grade Math Tutor
MGI/GEAR UP, CUNY Hunter College Leanne Stahnke
East Side Community HS Giselle George
New York, NY

RESEARCH EXPERIENCE:

7/08 – Graduate Research Assistant
Chemistry Dr. Munira Khalil
University of Washington, Seattle, WA

9/07 – 7/08 Research Assistant
Chemistry Dr. Fernando Raineri
SUNY at Stony Brook, Stony Brook, NY

5/06- 4/07 Technician B
Pathology Dr. Ila Singh
Columbia University Medical Center, New York, NY

9/02- 8/04 Research Student
Chemistry Dr. Stanislaus S. Wong
SUNY at Stony Brook, Stony Brook, NY

ADDITIONAL EXPERIENCE:

5/05- 5/06	Quality Control Engineer Sensitron Semiconductor, Deer Park, NY
2/01- 8/04	Technical Support Specialist Chemistry SUNY at Stony Brook, Stony Brook, NY

PUBLICATIONS:

Cheng, M., Brookes, J. F., Montfort, W. R., and Khalil, M., "The pH-Dependent Picosecond Structural Dynamics in the Distal Pocket of Nitrophorin 4 Investigated by 2D IR Spectroscopy." Journal of Physical Chemistry B, 2013.. http://dx.doi.org/10.1021/jp407052a

Lynch, M.S., Slenkamp, K.M., ***Cheng, M.*** and Khalil, M., "Coherent Fifth-Order Visible–Infrared Spectroscopies: Ultrafast Non-Equilibrium Vibrational Dynamics in Solution." Journal of Physical Chemistry A, 2012, 116 (26):7023. http://dx.doi.org/10.1021/jp303701b

Cheng, M.; Reynolds, A.; Widgren, H. and Khalil, M. "Generation of tunable octave-spanning mid-infrared pulses by filamentation in gas media" Optics Letters, 2012, 37 (11):1787. http://dx.doi.org/10.1364/OL.37.001787

Lynch, M.S., ***Cheng, M.***, Van Kuiken, B.E., and Khalil, M. "Probing the Photoinduced Metal-Nitrosyl Linkage Isomerism of Sodium Nitroprusside in Solution Using Transient Infrared Spectroscopy." Journal of the American Chemical Society, 2011, 133(14):5255. http://dx.doi.org/10.1021/ja110881n

Lynch, M.S., ***Cheng, M.***, Van Kuiken, B.E., Daifuku, S. and Khalil, M. "Uncovering Coherent and Incoherent Vibrational Interactions in a Transition Metal Mixed Valence Complex Using Femtosecond Two-Dimensional Infrared Spectroscopy." In Ultrafast Phenomena XVII, Oxford University Press, 2011, 346.

CONFERENCE PROCEEDINGS:

Cheng, M., Reynolds, A., Widgren, H. and Khalil, M. Development of a Tunable Ultra-Broadband Mid IR Pulsed Source for Nonlinear Spectroscopy. American Physical Society March Meeting 2012 Talk.

Cheng, M., Lynch, M.S., Khalil, M. Development of a Tunable Ultra-Broadband Mid-IR Source for Multidimensional IR Spectroscopy. Conference on Coherent Multidimensional Spectroscopy 2010 Poster.